EPA-600/2-77-229
November 1977

Environmental Protection Technology Series

TIME-OF-FLIGHT AEROSOL BEAM SPECTROMETER FOR PARTICLE SIZE MEASUREMENTS

Environmental Sciences Research Laboratory
Office of Research and Development
U.S. Environmental Protection Agency
Research Triangle Park, North Carolina 27711

RESEARCH REPORTING SERIES

Research reports of the Office of Research and Development, U.S. Environmental Protection Agency, have been grouped into nine series. These nine broad categories were established to facilitate further development and application of environmental technology. Elimination of traditional grouping was consciously planned to foster technology transfer and a maximum interface in related fields. The nine series are:

1. Environmental Health Effects Research
2. Environmental Protection Technology
3. Ecological Research
4. Environmental Monitoring
5. Socioeconomic Environmental Studies
6. Scientific and Technical Assessment Reports (STAR)
7. Interagency Energy-Environment Research and Development
8. "Special" Reports
9. Miscellaneous Reports

This report has been assigned to the ENVIRONMENTAL PROTECTION TECHNOLOGY series. This series describes research performed to develop and demonstrate instrumentation, equipment, and methodology to repair or prevent environmental degradation from point and non-point sources of pollution. This work provides the new or improved technology required for the control and treatment of pollution sources to meet environmental quality standards.

This document is available to the public through the National Technical Information Service, Springfield, Virginia 22161.

EPA-600/2-77-229
November 1977

TIME-OF-FLIGHT AEROSOL BEAM SPECTROMETER FOR PARTICLE SIZE MEASUREMENTS

by

Barton Dahneke
Radiation Biology and Biophysics
University of Rochester
Rochester, New York 14642

R803065

Project Officer
Charles W. Lewis
Atmospheric Chemistry and Physics Division
Environmental Sciences Research Laboratory
Research Triangle Park, North Carolina 27711

ENVIRONMENTAL SCIENCES RESEARCH LABORATORY
OFFICE OF RESEARCH AND DEVELOPMENT
U.S. ENVIRONMENTAL PROTECTION AGENCY
RESEARCH TRIANGLE PARK, NORTH CAROLINA 27711

DISCLAIMER

This report has been reviewed by the Environmental Sciences Research Laboratory, U.S. Environmental Protection Agency, and approved for publication. Approval does not signify that the contents necessarily reflect the views and policies of the U.S. Environmental Protection Agency, nor does mention of trade names or commercial products constitute endorsement or recommendation for use.

ABSTRACT

A time-of-flight aerosol beam spectrometer (TOFABS) is described. The instrument has been designed and constructed to perform in situ real time measurements of the aerodynamic size of individual aerosol particles in the range 0.3 to 10 μm diameter. The measurement method consists of (1) allowing a sample aerosol to undergo expansion through a nozzle into a vacuum chamber, such that each particle acquires a terminal velocity depending on its aerodynamic size, then (2) measuring the terminal velocity by determining the time taken for each particle to traverse a laser beam of fixed width. An experimental calibration curve relating time-of-flight and aerodynamic size, based on the use of polystyrene latex spheres, is shown to be in good agreement with a theoretical calibration obtained from the gas - particle dynamics equations. A comprehensive discussion of the properties and uses of aerosol beams is included as an appendix.

This report was submitted in fulfillment of Grant No. R803065 by the University of Rochester under the sponsorship of the U.S. Environmental Protection Agency. This report covers the period June 1, 1974 to February 28, 1977, and work was completed as of March 15, 1977.

CONTENTS

FIGURES

ACKNOWLEDGMENTS

The expert electronics assistance of Danny McFee, Joe Allen and Jeff Link is gratefully acknowledged. Their ability and energy in designing and perfecting the electronics circuitry was impressive. Partial support of this work in the form of equipment, supplies and salary support was provided by the University of Rochester Biomedical and Environmental Research Project which is supported by the U.S. Energy Research and Development Administration, and by a grant from the National Institute of Environmental Health Sciences. This support is also gratefully acknowledged. The appendix section will appear in Recent Developments in Aerosol Science, (D. Shaw, Ed.) John Wiley & Sons, Inc. (in press) and is included by permission of the publisher.

SECTION 1

INTRODUCTION

In recent years the physical and chemical properties of airborne particulates has become a subject of keen interest because of the increase in air pollution and the possible widespread effect on public health. However, the problem of measuring the size distribution (not to mention the chemical nature) of airborne particulates has proved quite difficult. Despite significant advances in measurement techniques and instruments obtained by the substantial efforts in many laboratories, there is presently no single instrument available that can monitor the size distribution of an aerosol over the full "respirable" size range, i.e., the particle size range between 0.01 and 5 μm diameter.

Aerosol beams seem useful in the measurement of airborne particulates because the particles are isolated from their suspending gas which allows use of sensitive detection and measurement techniques, such as mass spectrometry, and because the terminal velocity obtained by the particles in the vacuum chamber uniquely infers their "aerodynamic size", as described later in this report. Because this report focuses on the description of a particular aerosol beam instrument, we include as an appendix an article reviewing aerosol beams for the reader with broader interest in this topic.

We proposed as the goal of this research to design and build a time-of-flight aerosol beam spectrometer (TOFABS) capable of rapid on-line measurement of the size distribution of atmospheric particles in the size range from ~ 0.5 to 10 μm diameter and to demonstrate the instrument by measuring example size distributions of the atmospheric aerosol.

The instrument has been built and operated. It can measure particle sizes in the range from 0.3 to 10 μm diameter. However, atmospheric aerosol size distributions were not measured because of insufficient time to build one final electronics item. This lack of time was due, in part, to unexpected difficulty encountered in the development of the electronics components and

in part to an unfortunate reduction in the project support due to an unanticipated shift of Agency funds causing the project to be terminated six months early. Evaluation of the instrument was therefore performed with laboratory aerosols.

SECTION 2

CONCLUSIONS AND RECOMMENDATIONS

1. The TOFABS technique provides a fast, on-line method for sizing airborne particulates. When the particle density is known, the sizing is accurate. For particles of unknown mass density, an inherent uncertainty in particle size exists which can be substantial. This sizing technique has the advantage that particles are not removed from the beam but are available to subsequent measurement of, say, composition.
2. The measurement of particle TOF in a TOFABS would be more simply and accurately accomplished by detecting the beam particles at two locations of known separation rather than with a single detector as in the present design. The advantage of the two detector method lies in the simpler electronics required. For example, linear (analog) signal processing is not required as in the present electronics system so that pulse compression is not needed. With two separated detectors the TOF could be measured using pure logic components regardless of whether the signal pulse was amplifier chopped. Almost all of the electronics developed for the present TOFABS system are directly usable in this type of system. An important advantage of the present instrument, namely small coincidence error levels due to the short time required to measure the particle TOF, can be retained in a dual detector system if two separate detectors are used to provide start and stop signals to the TOF counters. Parallel counters would allow counting of more than one particle simultaneously passing between the detectors. In the event coincidence errors may be significant due to faster particles overtaking slower ones between the detectors, the addition of a third detector and suitable gating circuitry could be used to eliminate coincidence errors altogether. However, this third detector does not seem necessary unless long flight paths between detectors are used and concentrated aerosols are being measured.
3. Even when operated in a "two location" mode, as indicated in 2., particle

sizing in a TOFABS by optical methods cannot be strongly recommended because

a. the laser light source, PMT and associated equipment are expensive,

b. this equipment is not well suited for field measurements because of its power requirements, cooling water requirements, fragility, and the susceptibility of the optical components to contamination by dust and other deposits, and

c. the huge variation in optical signal with particle size can present difficult problems.

4. A novel method of particle detection more suitable for use in a TOFABS, including use in field models, may be the charging of the aerosol beam particles in a crossed electron beam with subsequent particle detection by electron beam scattering as the charged particle passes through other electron beams. The feasibility of this method is investigated in the Appendix. The electron beam method presents an added benefit, namely, the possibility of electrostatically focusing the aerosol beam. This method is being further investigated in our laboratory.

SECTION 3
SYSTEM DESIGN

The basic operation of the TOFABS system comprises the expansion of a sample aerosol through a nozzle into a vacuum chamber. Within the vacuum chamber the aerosol beam particles pass through a focused laser beam. Each particle thus generates a scattered light signal seen by a photomultiplier tube (PMT) which converts the scattered light signal into an electronic signal. Because the velocity attained by each particle in its acceleration through the nozzle-free jet expansion of the aerosol depends on the particle aerodynamic size, the size may be inferred from a measurement of the particle's time-of-flight (TOF) through the light beam. The intensity of the scattered light signal is not used to infer particle size, as in optical type sizing instruments.

Details of the system design and operation are given in the following sections. As the system incorporates vacuum, optical and electronic components the description is organized under these headings.

VACUUM SYSTEM AND SAMPLE INLET

The aerosol beam was generated by expansion of the aerosol sample through a converging nozzle of 0.2 mm throat (exit plane) diameter having the geometry shown as nozzle 1 of Fig. 1. The aerosol sampling rate was 100 cc/min entrained into the central core of a flow of clean, dry air through the nozzle. The total flow through the nozzle was 342 cc/min. The aerosol sample being confined to the central core of the expanding jet provided an aerosol beam having substantially smaller solid angle. Thus, the beam particles passed through the center of the laser beam giving uniform signals for similar particles.

The vacuum chamber is shown to scale in the diagram of Fig. 2. Of course many details are omitted for the sake of clarity, such as the plug of the bottom hole and the exhaust hole to the vacuum pumps located on the back surface, right hand side, midway between top and bottom. The size scale of the

diagram can be taken from the bottom hole which has a diameter of 2.54 cm.

The system was pumped by two Alcatel mechanical pumps type ZM2012 having a combined pumping capacity of 600 liters/min. These pumps maintained a vacuum chamber pressure of 0.7 Torr as measured on a pair of Hastings Vacuum Gauges, Models VT-4 and VT-6. Two gauges were continuously used to provide a cross-check and to provide high resolution in complimentary ranges.

OPTICAL SYSTEM

The source of the focused laser beam was a Spectra-Physics Model 164-03 Argon laser tuned to 488.0 nm wavelength. Although the laser was capable of producing more than 1 Watt of power at this wavelength, it was operated at an output power of 400 mW.

The laser beam was cleaned by passing it through a spatial filter (Gaertner Scientific Corporation, Chicago) incorporating a 10X microscope objective, a 25 μm pinhole and a 20X microscope objective.

The laser beam was then directed by means of two reflectors, which allowed adjustment of the laser beam height and direction. The beam next passed through an iris diaphragm to stop scattered and reflected light from the lenses and reflectors, except that which was nearly on axis.

The laser beam entered the vacuum chamber through a planoconvex cylindrical lens (Klinger Scientific, #318851) having 100 mm nominal focal length. This lens served as a window to the vacuum chamber and focused the laser beam in one dimension (the vertical). The plane surface was inclined 45° to the laser beam to cause internal reflections to be separated from the primary beam so they could be easily stopped. The intersection length for this lens is normally 94.5 mm but because the lens was inclined to the light beam axis the intersection distance was about 77 mm. This intersection distance caused the laser beam to reach its one-dimensional focus at the aerosol beam axis, as shown in Fig. 2. The horizontal width of the laser beam at this point was approximately 2 mm while its vertical thickness was about 100 μm.

Two sets of externally adjustable knife edge stops were located in the vacuum chamber between the cylindrical lens and the aerosol beam. These were used to clean the beam of scattered and reflected noise generated in the cylindrical lens and upbeam elements.

The laser beam light not scattered by aerosol beam particles passed through a hole 4x5 mm cut into the spherical mirror of Fig. 2 and on into a

light trap consisting of a bundle of needles located at the end of a threaded, blackened tube of 25 cm length. This light trap was able to absorb the 400 mW laser beam without detectable heating.

Light scattered by aerosol beam particles in the forward direction between about 2° and 25° angle with the beam axis was collected by the spherical mirror of Fig. 2 (Klinger Scientific, #340023) and focused onto the small plane deflector mirror also shown in Fig. 2. This latter mirror diverted the scattered light signals out the side of the vacuum chamber through a pair of biconvex lenses (Klinger Scientific, #311138) which focused the scattered light signals onto the cathode of the photomultiplier tube (ITT Model FW-130).

Since the light intensity distribution was Gaussian across the focused laser beam, the PMT output signals should be Gaussian in time as each particle traversed the laser beam at constant velocity, provided the particle size was small compared to the laser beam thickness. The upper oscilloscope trace of Fig. 3 shows an example PMT signal which is indeed Gaussian.

To measure particle TOF across the beam, i.e., across a fraction of the beam of fixed path length, it was necessary to turn on a counting system over the duration for which the PMT signal exceeded a fixed fraction of the signal peak. This process of "normalizing" the signal pulses was necessary because variations in particle size, orientation and index of refraction can cause changes in the pulse width, but not in the normalized pulse width.

Of course several equivalent electronics schemes can be used to accomplish this result. The electronics system we designed is described in the next section.

ELECTRONIC SYSTEM

The PMT output signal is regarded as the input signal of the electronics system shown schematically in Fig. 4. Not shown is a preamplifier circuit (line driver) that boosts the power of the PMT output. This line driver circuit is shown in Fig. 5.

The basic operation of the electronics system is as follows. After amplification the signal reaches a peak detector whose output is divided by a resistor chain to a constant fraction (namely 1/3) of the peak signal voltage. This constant voltage level is provided as the reference level of the analog comparator. The same amplified input signal, delayed 0.5 μsec, is the test

input of the analog comparator. The analog comparator output is therefore at the low logic level except for the duration for which the delayed signal exceeds 1/3 of its maximum amplitude, as shown by the lower trace of Fig. 3. That is, the analog comparator output gives a high level logic signal for the duration of the particle TOF across a fixed fraction of the laser beam thickness. The TOF of each particle is therefore measured for the same path length.

The output of the analog comparator triggers an AND gate, provided the amplified PMT signal exceeds an adjustable noise level determined by the reference input of the lower analog comparator of Fig. 4. Thus, PMT or amplifier noise is prevented from triggering the AND gate.

When the AND gate is triggered to the high logic level the particle TOF through the laser beam is digitally counted on the binary counter driven by the 64 MHz oscillator. Thus, the digital number accumulated in the binary counter is incremented every 15.6 nsec. The resolution in particle TOF is therefore better than 15.6 nsec.

When the particle passes out of the light beam the analog comparator output drops to the low logic level causing the contents of the binary counter to be transferred to a buffer storage (parallel load shift register), not shown in Fig. 4. The circuit is then reset and ready to count the TOF of the next particle while the further electronics continues to process the TOF data for the last particle.

To determine the size sub-range of the particle from the measured TOF, the digital TOF number in the buffer storage is compared by means of a binary comparator to the various numbers (sub-range limits) stored in the size range ROM. When the correct size sub-range is obtained, a single count is added to the size range counter corresponding to that sub range.

The size range counters are continually scanned and their contents displayed on an oscilloscope. Their contents can also be printed out with a Teletype printer. An example oscilloscope display obtained from a polydisperse NaCl aerosol is shown in Fig. 6.

Complete details of the electronics system are shown in Figs. 7-17 on which all components of the system are identified. The operation of the electronics is illustrated by the timing diagram of Fig. 11, where signals corresponding to the identified points throughout the circuitry are shown.

The effort we expended in the development of this electronics system

was substantial. It comprised by far the majority of our effort.

In the meantime microprocessor systems have become commercially available which can perform many of the functions of our electronics system. However, the microprocessor systems of which we are aware are all far too slow to be used in our system as presently constituted.

SECTION 4

CALIBRATION

The calibration curve relating particle size and TOF is needed to obtain the particle size distribution from the measured TOF data or to program the size range ROM to give TOFABS output as the particle size distribution directly. This curve was obtained in two ways, analytically and experimentally, described in the following sections.

ANALYTICAL CALIBRATION

The motion of a particle or droplet whose mass m_p may be changing due to condensation or evaporation is described by the equation of motion

$$m_p \frac{dv_p}{dt} = - \left[f + \frac{dm_p}{dt}\right] (v_p - v_f) \qquad [1]$$

and the energy equation

$$\frac{d(m_p c_p T)}{dt} = \lambda \frac{dm_p}{dt} - q \qquad [2]$$

where v_p is the particle velocity, v_f the local velocity of the surrounding fluid (calculated by ignoring the presence of the particle), t the time, f the particle's friction coefficient, c_p the specific heat of the particle material, T the particle temperature (assumed uniform), λ the latent heat of condensation or evaporation, and q the rate at which heat is being transmitted from the particle to the fluid.

The particle's friction coefficient is

$$f = 6\pi\mu a \kappa / C_s \qquad [3]$$

where μ is the fluid viscosity, a the particle radius, κ the dynamic shape factor and C_s the slip correction factor

$$C_s = 1 + Kn[1.234 + 0.414 \exp(-0.876/Kn)], \qquad [4]$$

Kn being the Knudsen number ℓ/a where ℓ is the mean-free-path of the fluid

molecules. For non-spherical particles the value of a must be adjusted in this latter expression to give the proper correction C_s. For spherical particles the factor κ is approximated within a few percent by

$$\kappa = 1 + 0.1062\ \mathrm{Re}^{0.8561},\quad \mathrm{Re} = 2a|v_f - v_p|/\nu \qquad [5]$$

where ν is the kinematic fluid viscosity. For non-spherical particles an additional shape factor must be included in κ.

The solution of [1] is

$$v_p(t) = e^{-\int_o^t \alpha(t)dt}\left[v_{fo} + \int_o^t e^{\sigma=\int_o^\tau \alpha d\sigma}\ \alpha(\tau)v_f(\tau)d\tau\right] \qquad [6]$$

where v_{fo} is the fluid (and particle) velocity at the nozzle entrance $x = 0$ and $t = 0$ and where

$$\alpha = (f + \frac{dm_p}{dt})/m_p. \qquad [7]$$

The particle location at time t is given by

$$x(t) = \int_o^t v_p\ dt. \qquad [8]$$

The following procedure is used to calculate the velocity of a particle as it accelerates through a nozzle system into a vacuum chamber. First, the steady state fluid velocity field $v_f(x)$ is calculated for the given nozzle system. Second, for a specific particle size, shape and mass, [6] and [8] are solved to obtain v_p vs. x. In practice, to prevent underflow and overflow errors from occurring in the computer calculations, [6] and [8] are solved in an iterative scheme, viz.,

$$v_p(t+\Delta t) = e^{-\int_t^{t+\Delta t}\alpha dt}\left[v_p(t) + \int_t^{t+\Delta t} e^{\int_t^{t+\Delta t}\alpha dt}\ \alpha(t)\ v_f(t)\ dt\right] \qquad [9]$$

$$x(t+\Delta t) = x(t) + \int_t^{t+\Delta t} v_p dt \qquad [10]$$

Furthermore, if Δt is sufficiently small so that $\alpha(t)$ does not change significantly over the interval between t and $t+\Delta t$, then

$$v_p(t+\Delta t) - v_p(t) = [v_f(t) - v_p(t)](1 - e^{-\alpha(t)\Delta t}). \quad [11]$$

With sufficiently small Δt, [10] and [11] can be used with [2] to obtain the v_p vs. x curve for a particle without incurring underflow - overflow problems.

Example results showing particle time-of-flight are shown in Fig. 1. Further calculated results showing the influence of nozzle diameter and of particle density are shown in Figs. 18 and 19.

EXPERIMENTAL CALIBRATION

To obtain an experimental calibration curve, monodisperse latex aerosols were generated and the PMT signals like that of the upper trace of Fig. 3 were measured. For each particle size the width (TOF) of the Gaussian pulse at 1/3 the maximum pulse amplitude was measured. These measured data are shown in Fig. 20.

The two measured values at 0.81 μm diameter were obtained for two batches of Dow latex spheres, both identified as 0.81 μm nominal diameter. Our measurements suggest that one batch had particle diameters slightly higher and the other batch slightly lower than 0.81 μm.

Since the exact thickness of the laser beam was not known, the analytical and experimental calibration curves could not be directly compared. However, they were combined by assuming a light beam thickness of 72 μm, which gave the best agreement of the two curves. This value of the light beam thickness, between points where the intensity is 1/3 the maximum (axial) value, agrees well with the estimated laser beam thickness of 100 μm between points where the intensity is $1/e^2$ or 13.5% of the axial value. The curve shown in Fig. 20 is the analytical calibration curve for an assumed laser beam thickness (flight path) of 72 μm. The good agreement of the calculated and measured data suggests the validity of the calibration curve.

SECTION 5
RESULTS

The TOFABS described in the preceding sections was used to measure various laboratory aerosols and the ambient atmospheric aerosol in the laboratory. Some experience in its use was thereby obtained.

The TOFABS was found to work well in the measurement of monodisperse and nearly monodisperse aerosols. To make these measurements the high voltage to the PMT was adjusted so that the amplified PMT output signals lay in the range between 0.1 and 10 volts. The lower limit corresponded approximately to the noise level while signals above the upper limit were "chopped" by the input amplifiers.

It was therefore not possible to measure the size distribution of moderately or highly polydisperse aerosols unless various PMT voltages were used in a sequence of measurements. The strong dependence of pulse height on particle diameter allowed only a relatively narrow size sub-range to be measured at one PMT voltage level.

We intended to solve this problem by the addition of a final electronics element to the system, namely, a "pulse compressor" that would compress pulses of a large range of amplitudes to pulses having a small variation in amplitude. Pulse compression would not affect the particle TOF measurement provided compression was obtained by linear amplification or attenuation of the pulse, since the pulse was effectively normalized by the electronics system anyway.

A possible design of the pulse compressor is shown schematically in Fig. 21. Unfortunately, the Agency supporting this project experienced an unexpected shift of funds and had to discontinue support of this project before this pulse compressor could be built. Measured data for highly polydisperse aerosols including atmospheric aerosols were therefore not obtained.

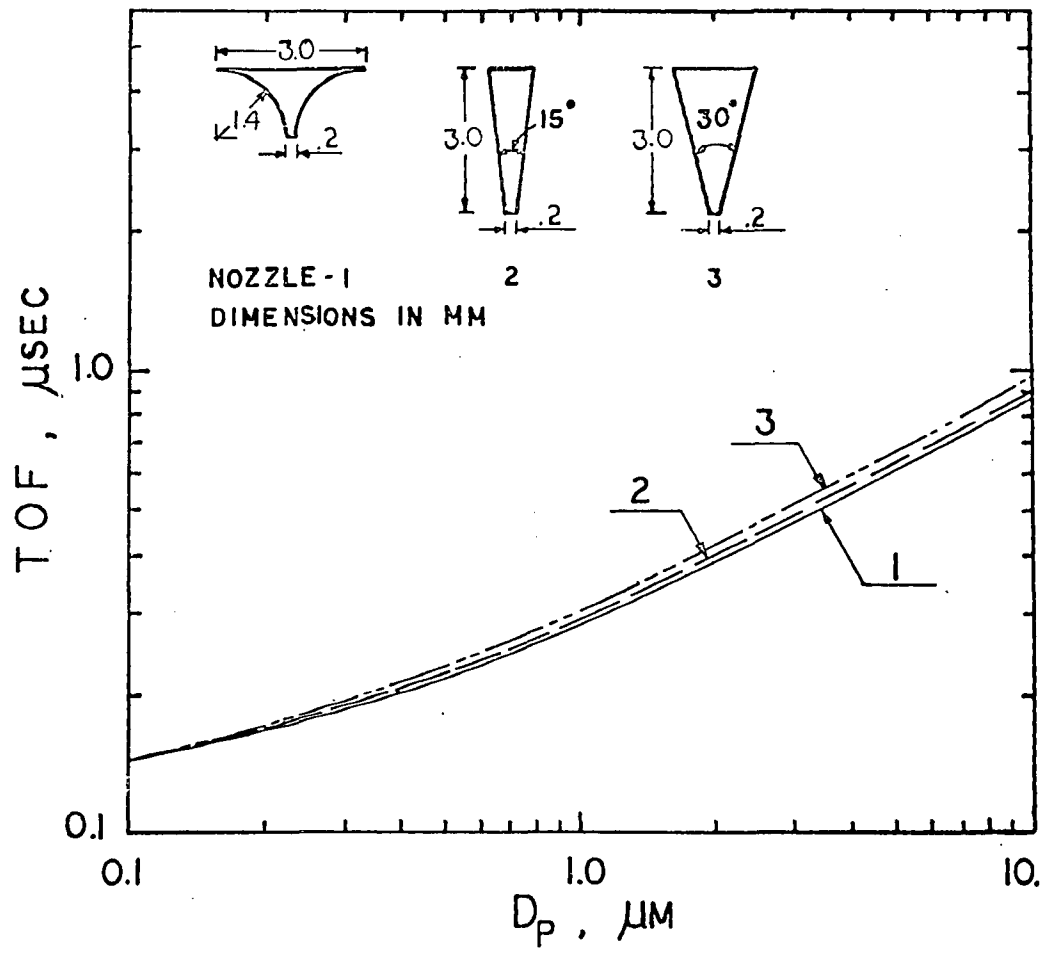

Figure 1. Calculated particle TOF across a flight path of 100 μm beginning 2 mm from the nozzle exit vs. particle diameter for beams of unit density spheres. The aerosol beam was assumed generated by expansion of an air aerosol at NTP through the three nozzles specified.

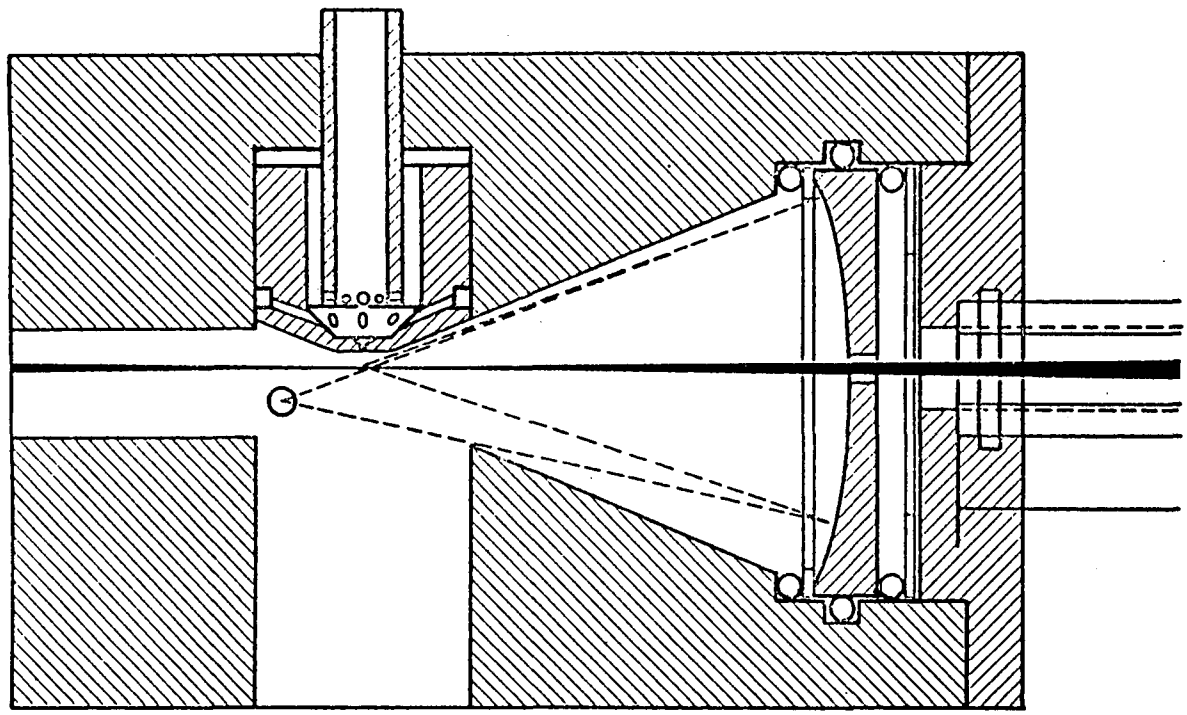

Figure 2. Diagram of the vacuum-optical chamber. The vertical aerosol beam intercepts the horizontal laser beam at its focus causing light to be scattered into the spherical mirror.

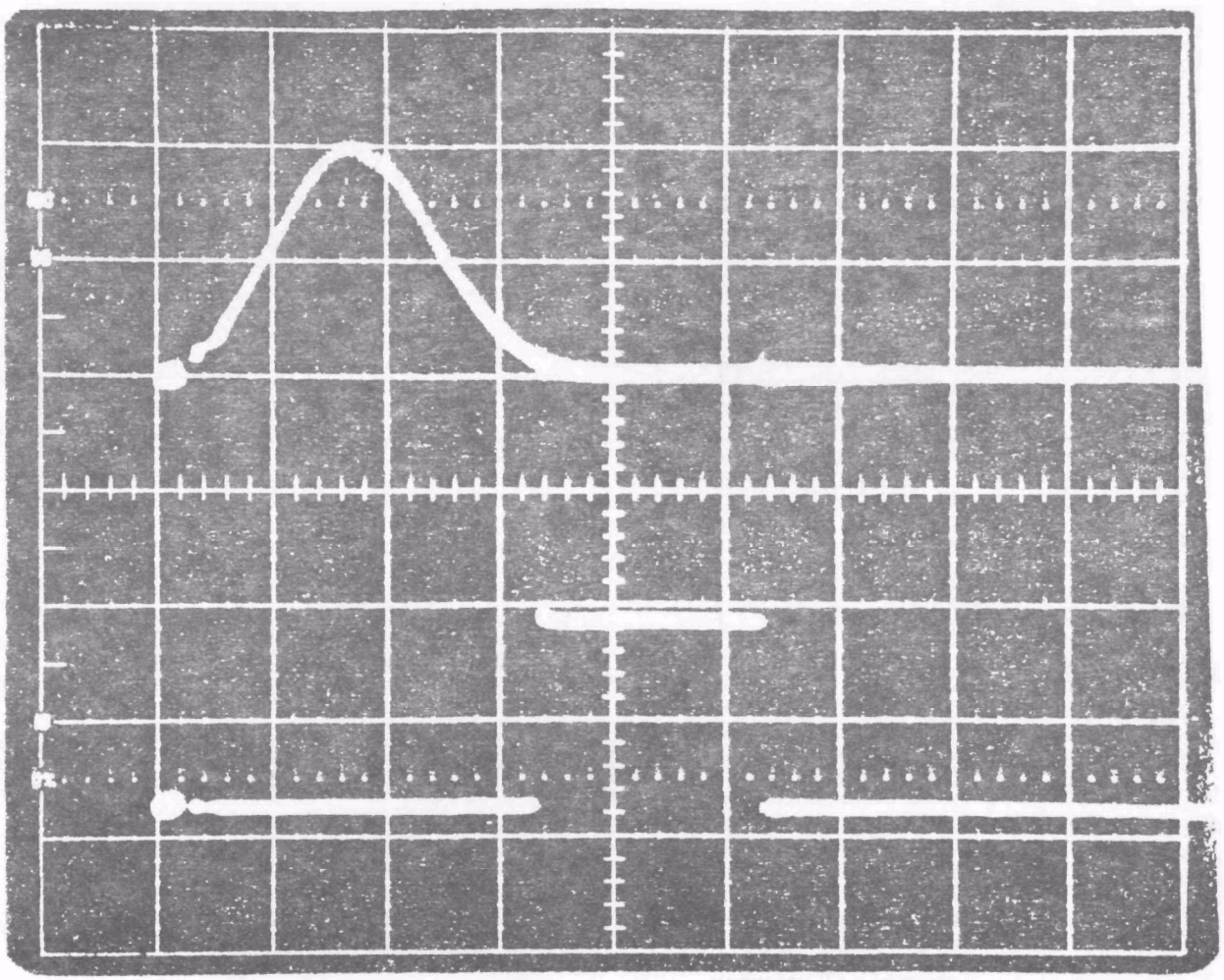

Figure 3. Upper trace: superimposed PMT signals generated by the scattered light signals of 2.02 μm diameter latex spheres traversing the focused laser beam. The horizontal scale is 0.2 μsec per cm.
Lower trace: superimposed logic pulses of fixed amplitude and width equal to the TOF of the 2.02 μm particles "through" the laser beam. The logic pulse time scale is delayed 0.5 μsec relative to the PMT signal.

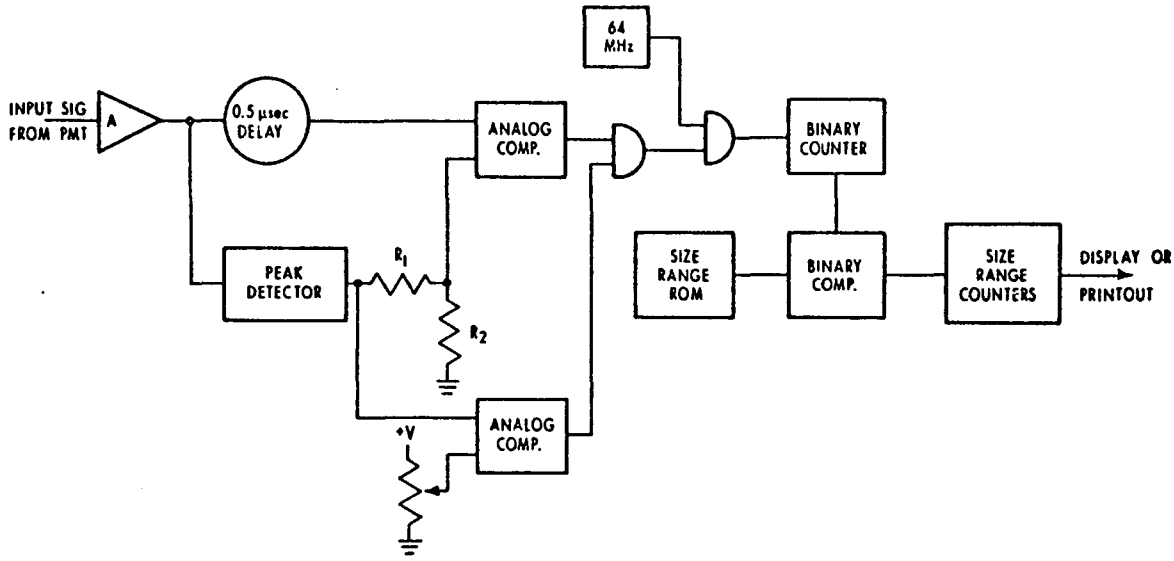

Figure 4. Schematic diagram of the electronics system.

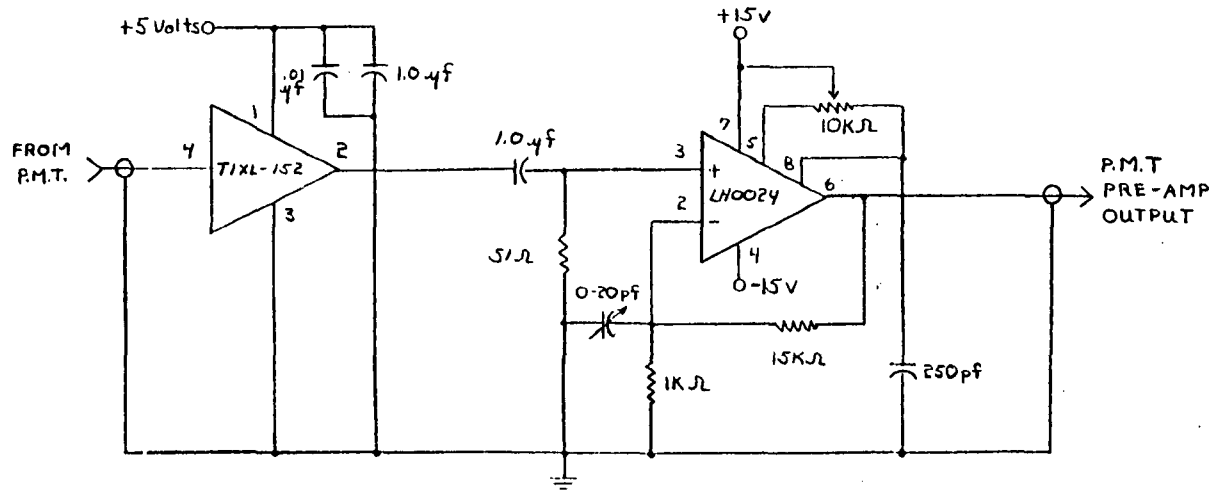

Figure 5. Pre-amplifier (line driver) circuit.

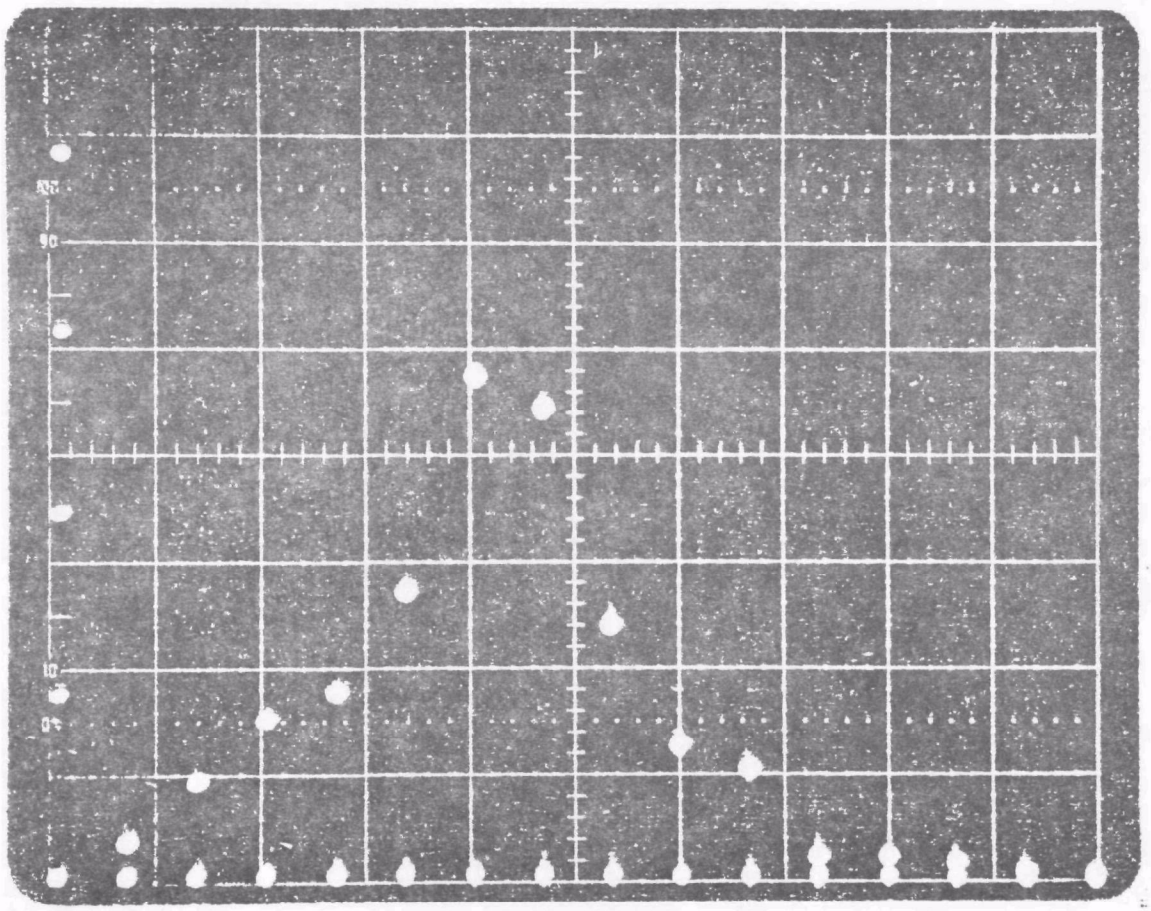

Figure 6. Example display of a measured TOF distribution for a polydisperse NaCl aerosol. The vertical axis represents the number of particles (counts) per TOF sub-range while the horizontal axis represents particle TOF. The maximum corresponds to an aerodynamic diameter of 0.9 μm, that is, a unit density sphere of this diameter will have the same TOF.

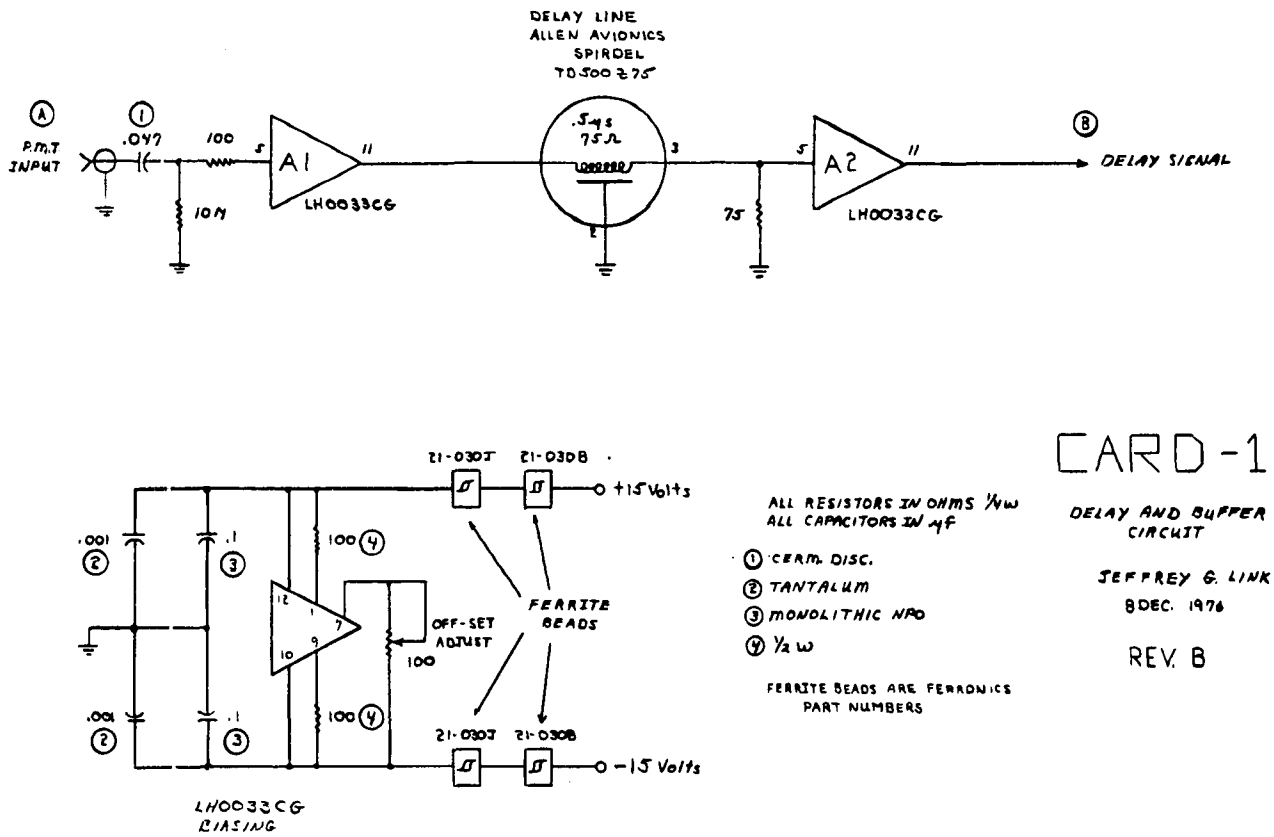

Figure 7. Delay and buffer circuit. Output signal B is delayed 0.5 μsec and is one-half the amplitude of input signal A (from the line driver circuit or PMT). Biasing circuitry for the buffer amplifiers is also shown.

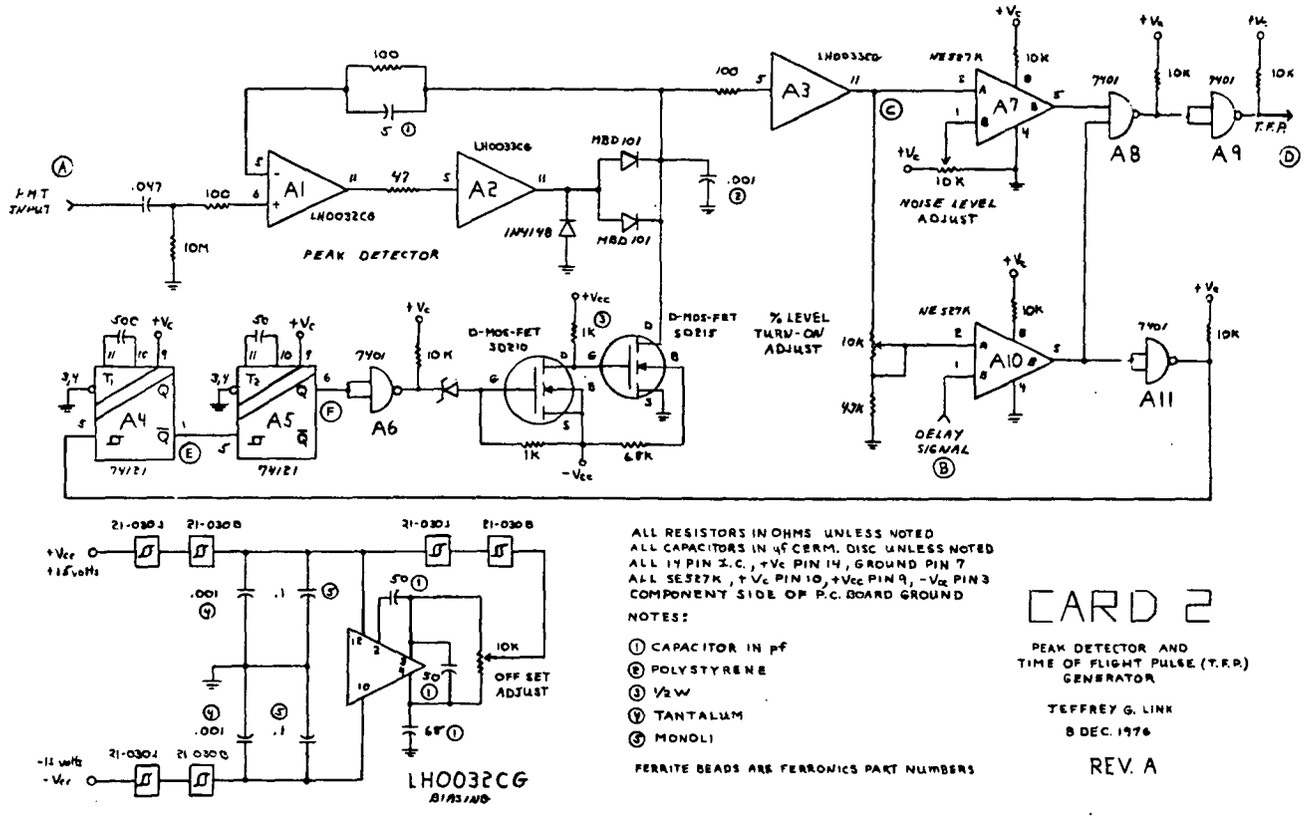

Figure 8. Peak detector and TOF pulse generator. Output pulse D is a logic pulse of width equal to the particle TOF through the laser beam.

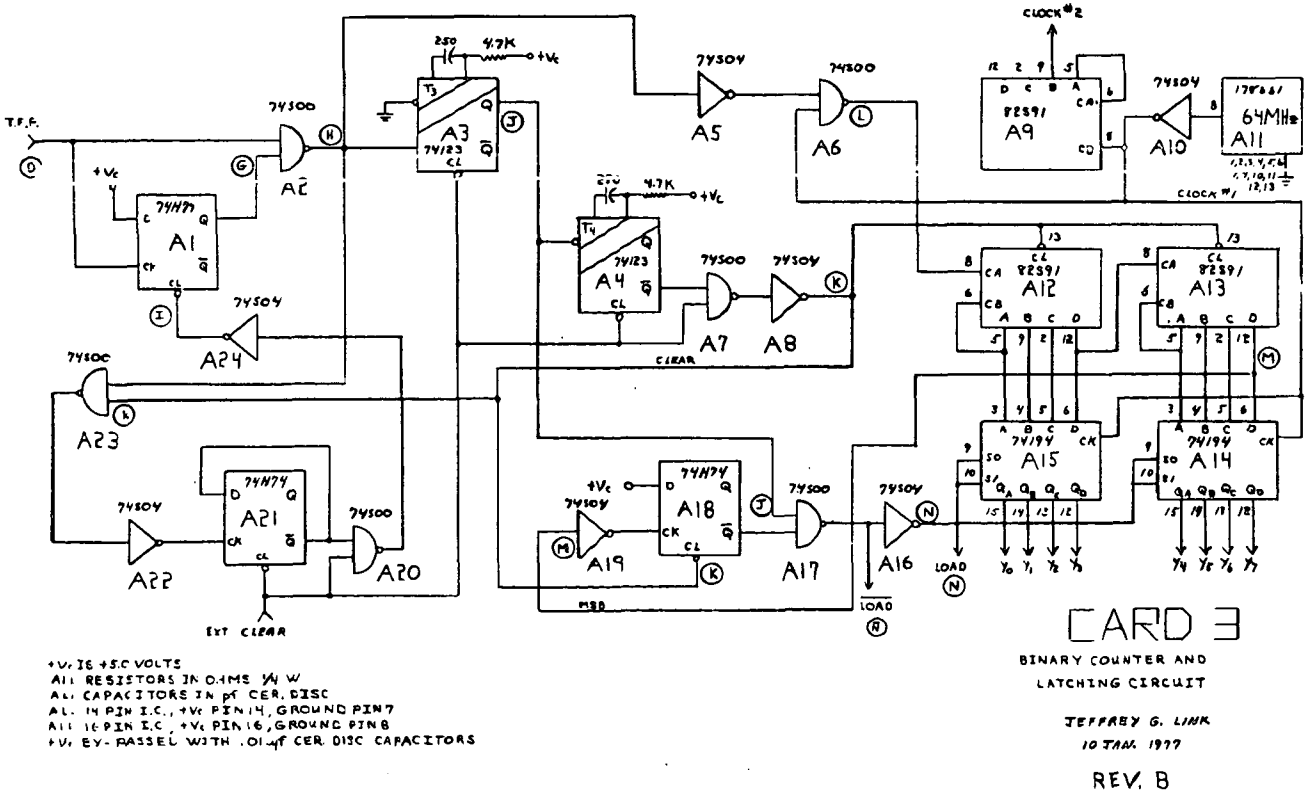

Figure 9. Binary TOF counter and buffer storage (latching circuit). The particle TOF is counted to 15.6 nsec resolution in the binary counter A12 and A13. The counted TOF is latched into the buffer storage A14 and A15 freeing the counter to count the TOF of the next particle.

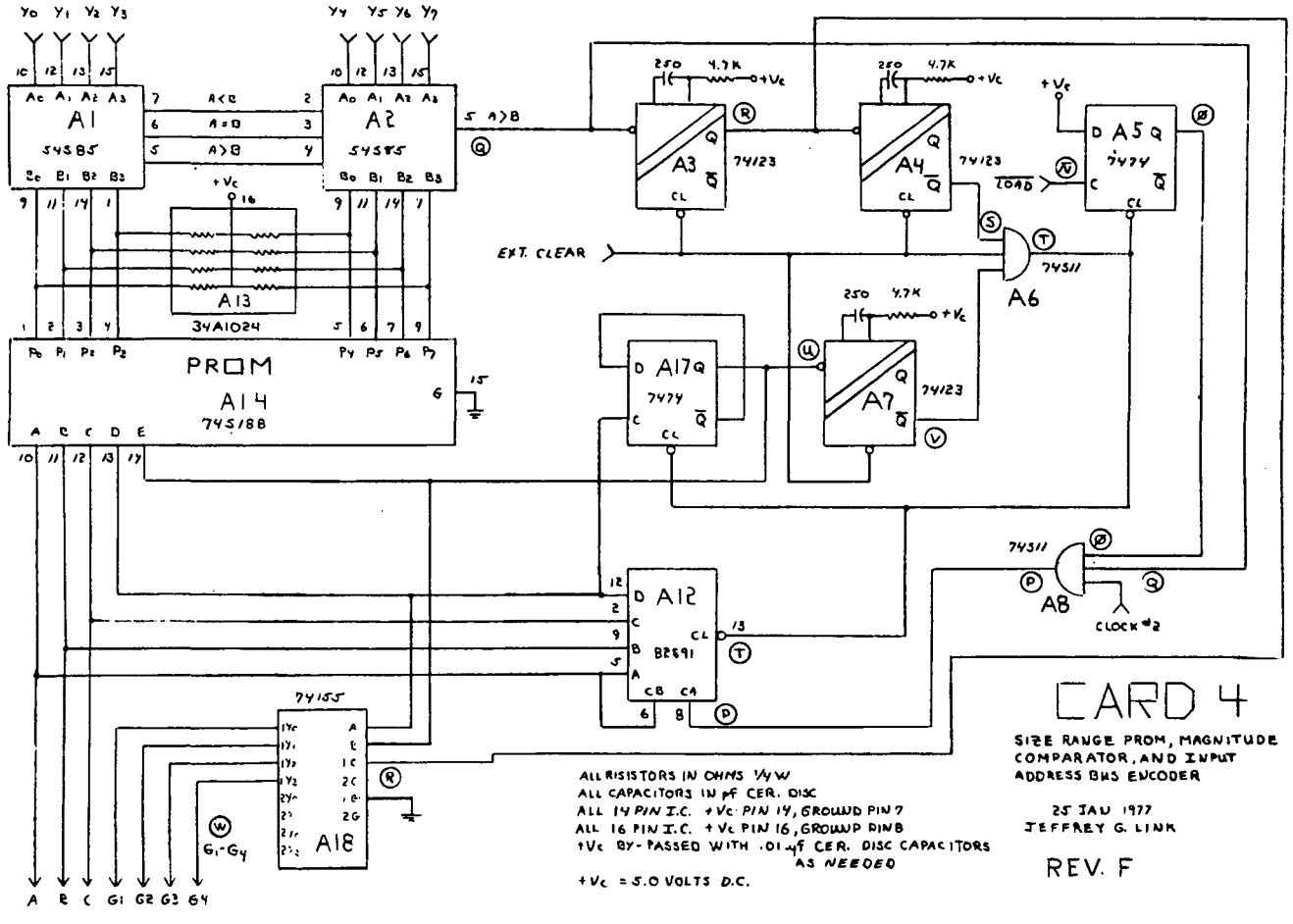

Figure 10. Size range calibration PROM, magnitude comparator and storage input address encoder. The PROM is coded through its various memory levels by clock #2 (16 MHz) and binary counter A12 and A17. When the contents of a PROM memory level (upper limit of a size sub-range) equals or exceeds the particle TOF in the buffer storage, the magnitude comparator output Q changes from high to low logic level, stopping the clock signal and causing a single count to be added to the contents of the proper binary counter (size sub-range channel).

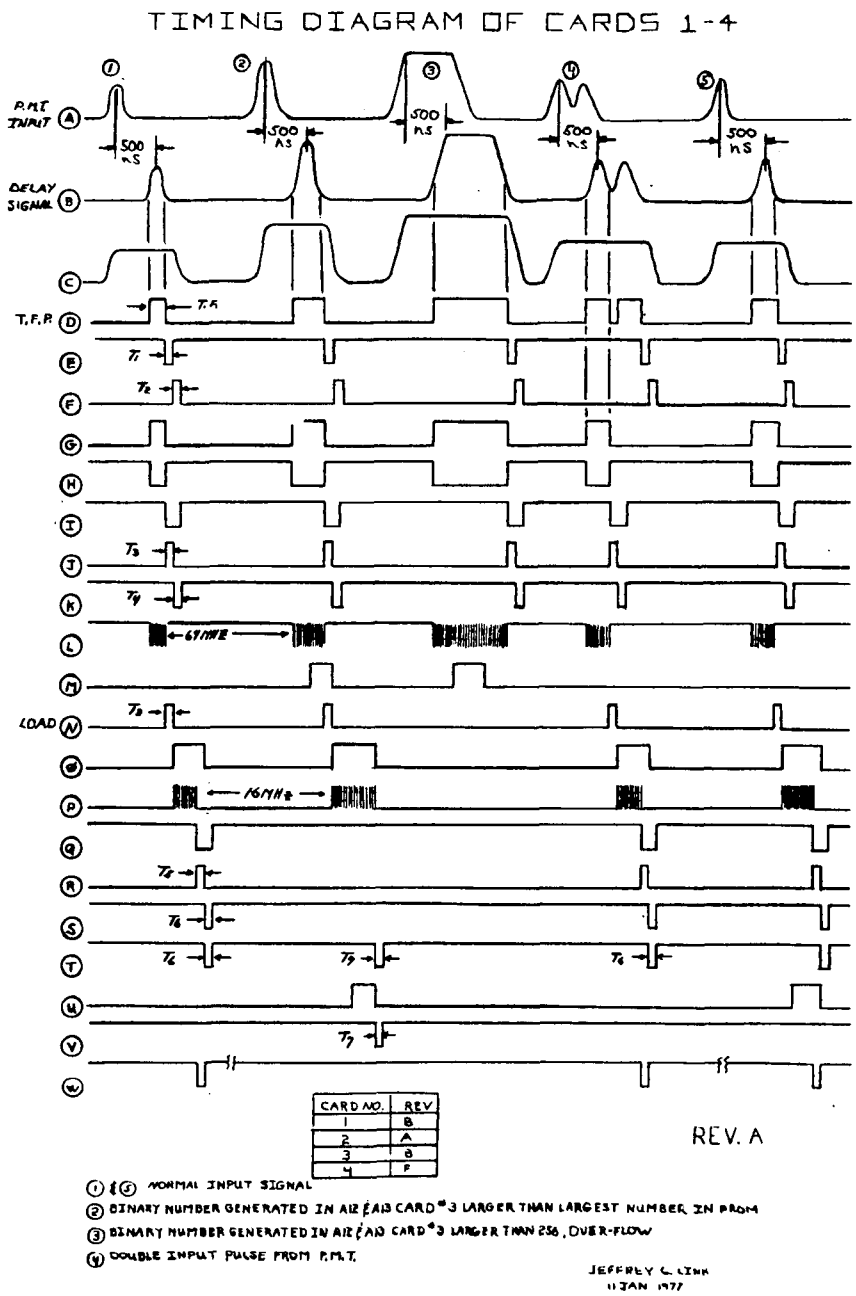

Figure 11. Timing diagram showing the sequence of pulses at various locations throughout the circuitry of Cards 1-4.

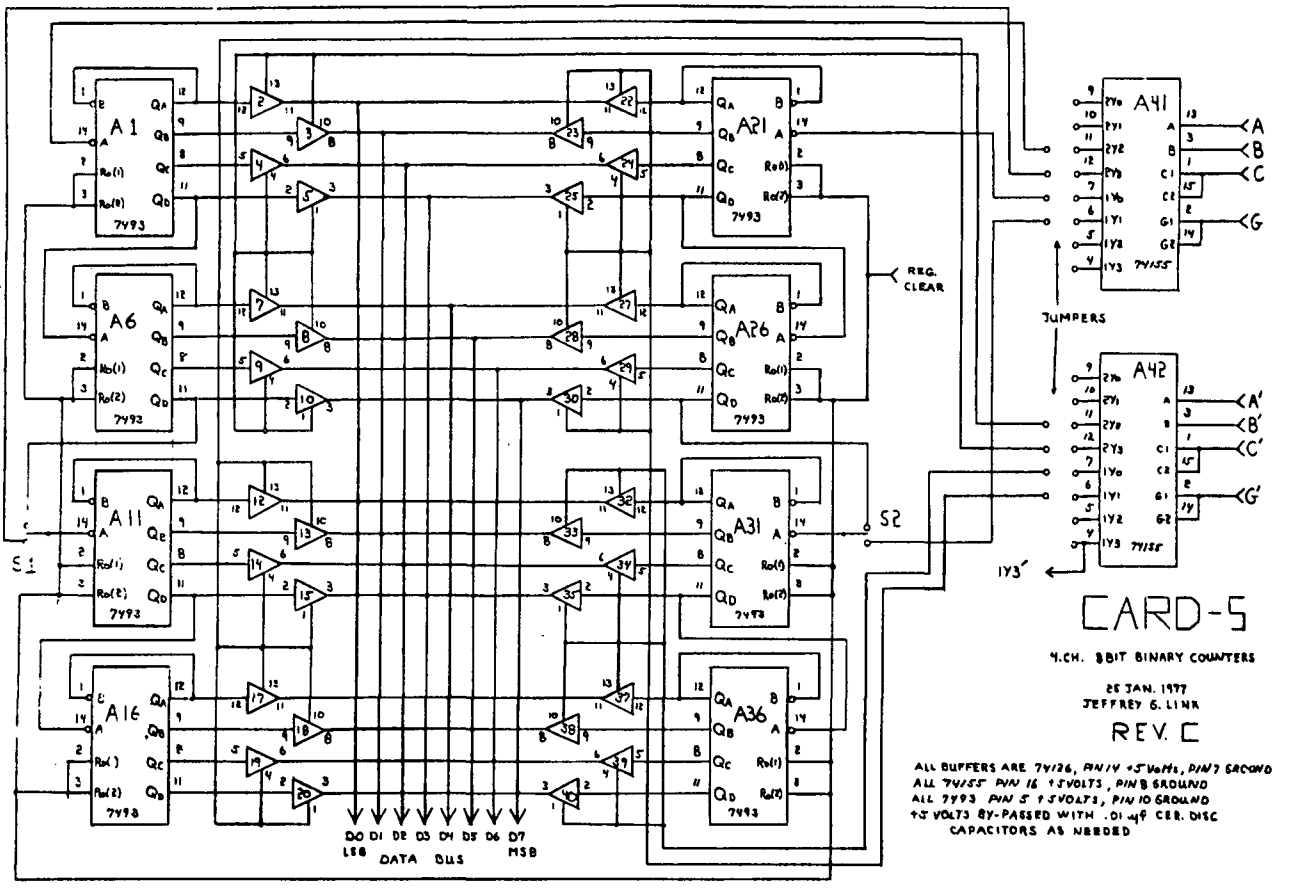

Figure 12. Size sub-range counters. Each card contains four 8-bit counters or two 16-bit counters. Each size sub-range channel can store either 0-255 counts or 0-65,535 counts. The capacity of each size sub-range channel can be selected as 8 or 16 binary bits. The storage capacity is thirty one 8-bit channels, minus one channel for each channel expanded to 16-bit capacity.

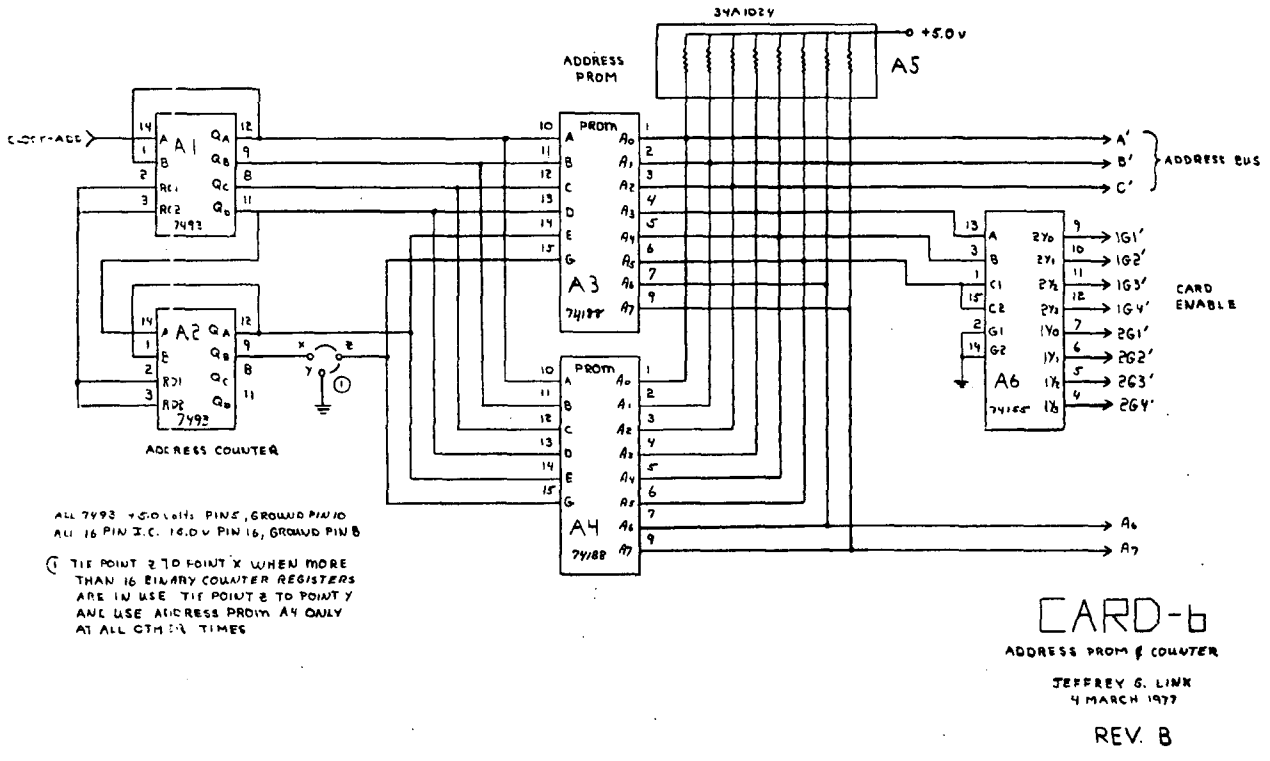

Figure 13. Address PROM for identifying the output address of the various size range channels. Since the output and input circuitry to each memory channel are independent, a separate output address PROM is used for data display and printout.

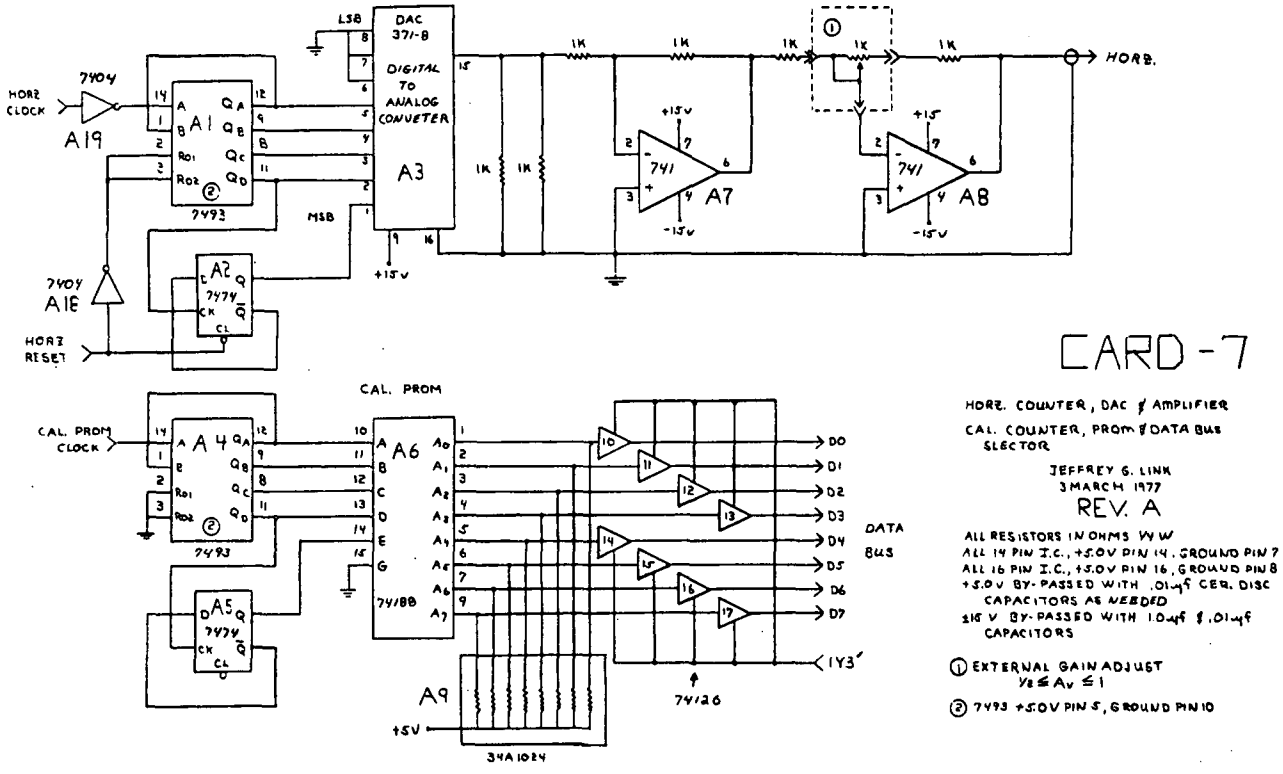

Figure 14. Horizontal control for visual data display. The PROM providing the vertical calibration marks is also shown.

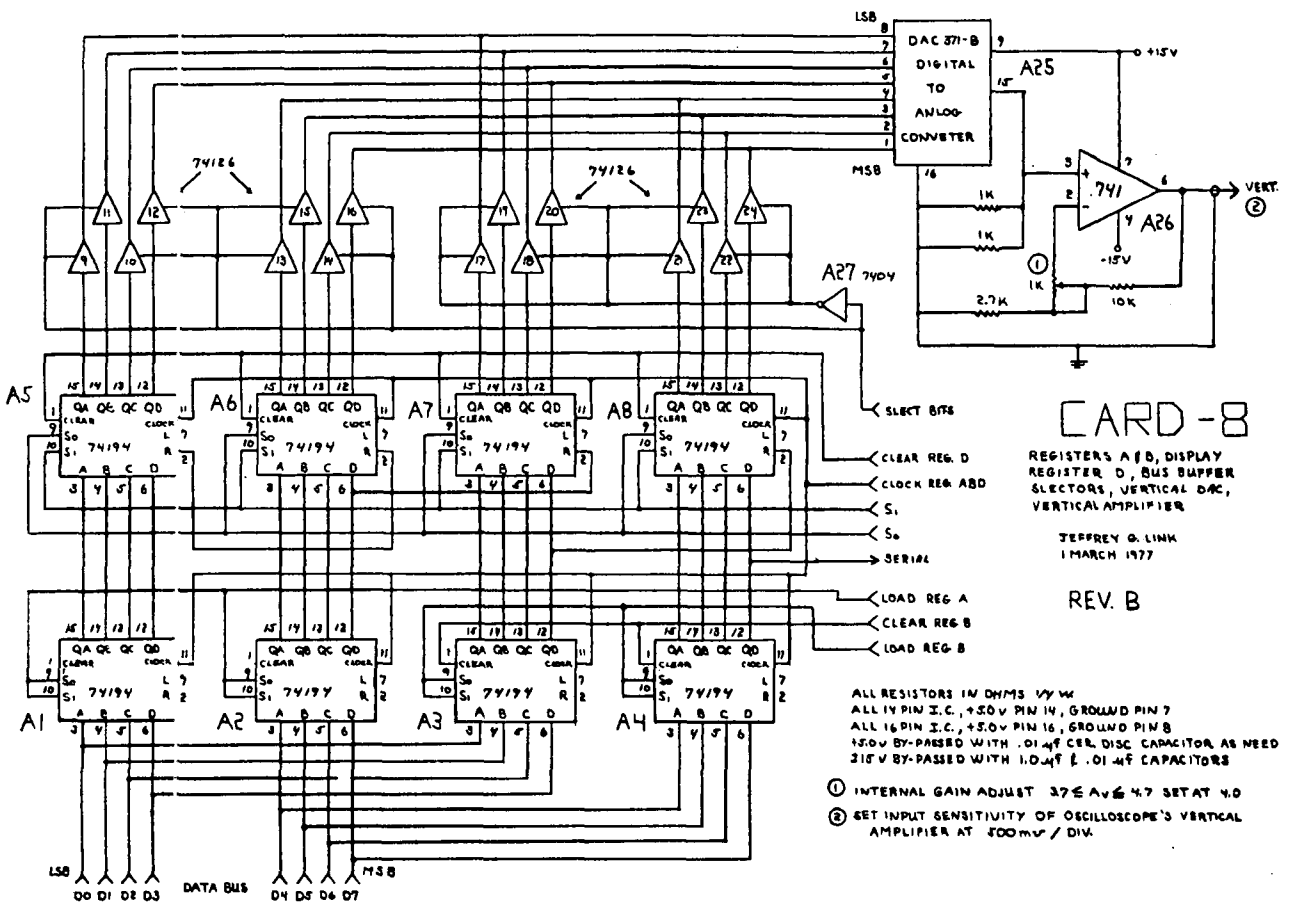

Figure 15. Circuitry for converting sequential 8-bit binary input to (a) parallel 16-bit binary output, (b) digital to analog converted output signal for visual display or (c) serial 16-bit binary output for printer.

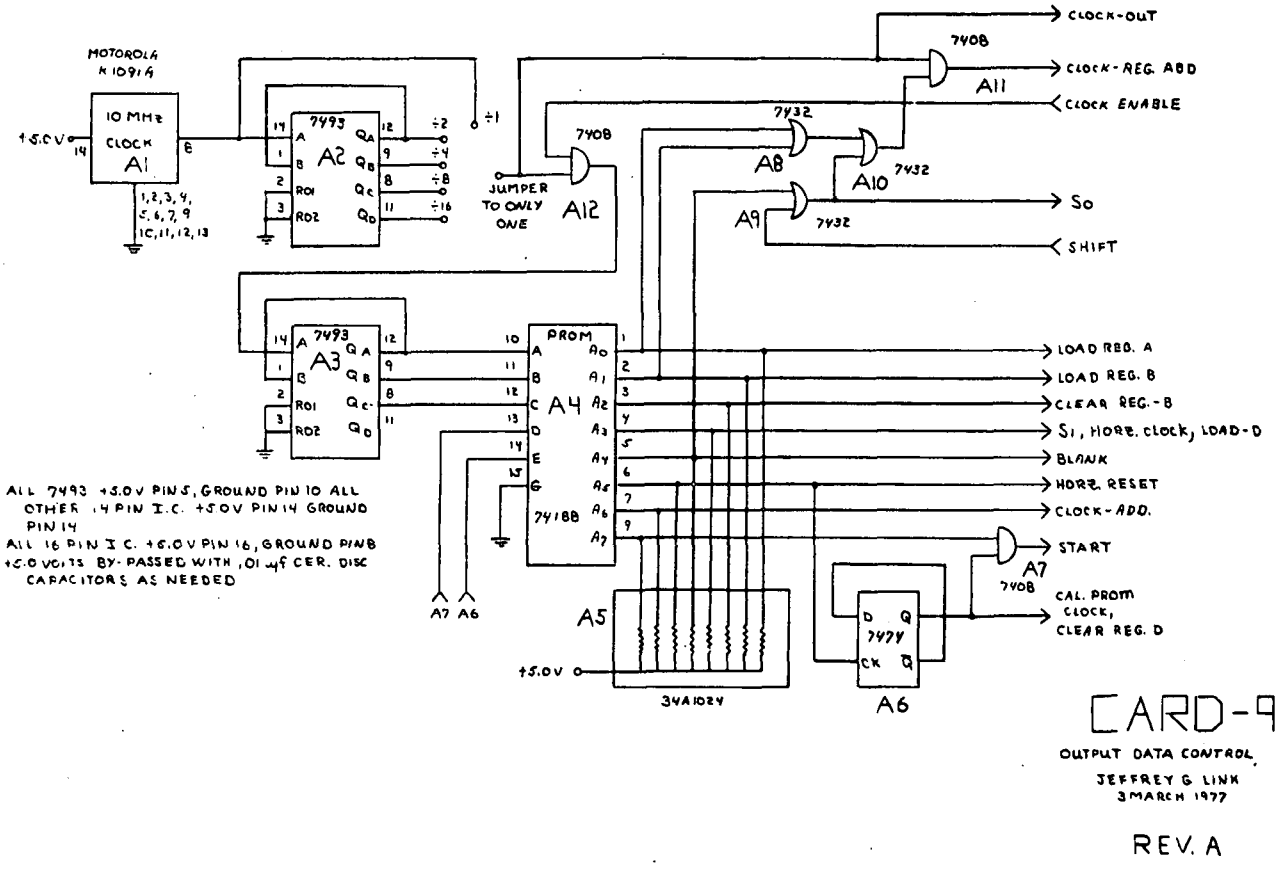

Figure 16. Output data control circuitry to control the operations of the circuitry of Cards 6, 7 and 8.

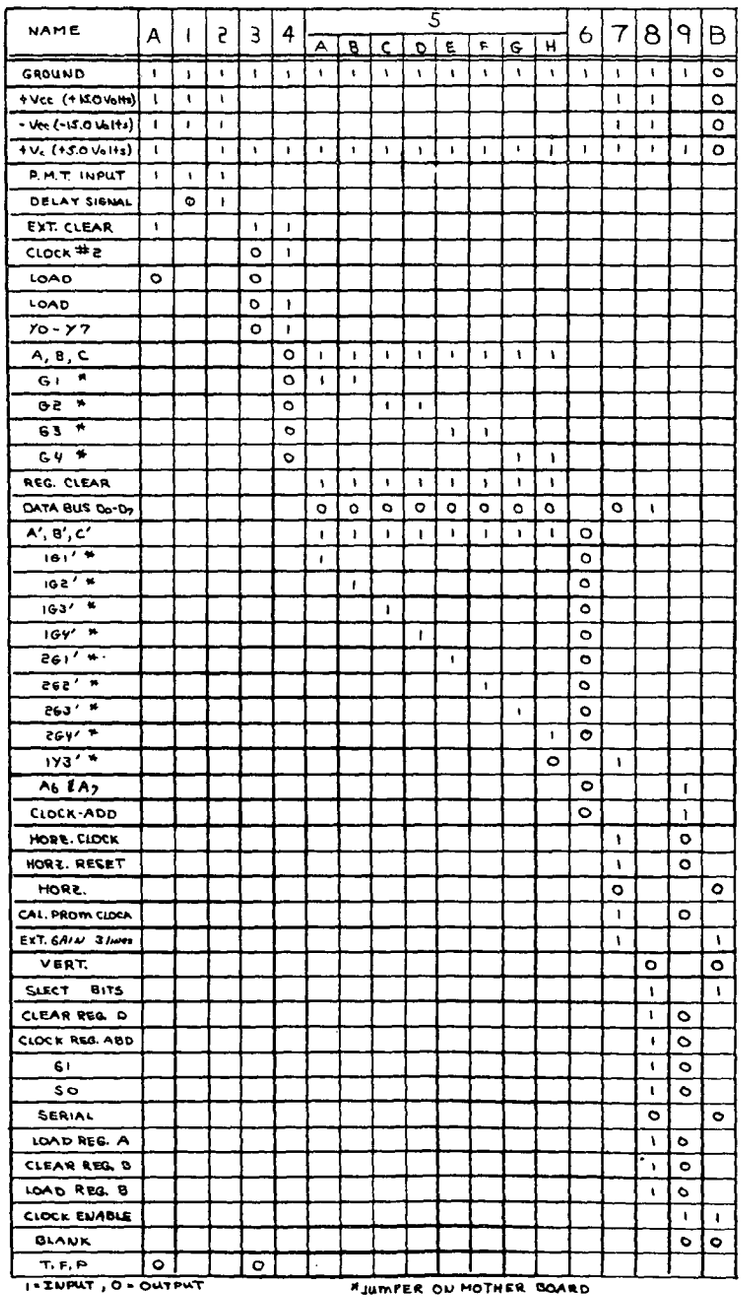

NAME	A	1	2	3	4	5 A	5 B	5 C	5 D	5 E	5 F	5 G	5 H	6	7	8	9	B
GROUND	1	1	1	1	1	1	1	1	1	1	1	1	1	1	1	1	1	0
+Vcc (+5.0 Volts)	1	1	1												1	1		0
-Vcc (-15.0 Volts)	1	1	1												1	1		0
+Vc (+5.0 Volts)	1		1	1	1	1	1	1	1	1	1	1	1	1	1	1	1	0
P.M.T. INPUT	1	1	1															
DELAY SIGNAL		0	1															
EXT. CLEAR	1			1	1													
CLOCK #2				0	1													
LOAD	0			0														
LOAD				0	1													
Y0 - Y7				0	1													
A, B, C					0	1	1	1	1	1	1	1	1					
G1 *					0	1	1											
G2 *					0			1	1									
G3 *					0					1	1							
G4 *					0							1	1					
REG. CLEAR						1	1	1	1	1	1	1	1					
DATA BUS D_0-D_7						0	0	0	0	0	0	0	0		0	1		
A', B', C'						1	1	1	1	1	1	1	1	0				
1G1' *						1								0				
1G2' *							1							0				
1G3' *								1						0				
1G4' *									1					0				
2G1' *										1				0				
2G2' *											1			0				
2G3' *												1		0				
2G4' *													1	0				
1Y3' *													0		1			
A_6 & A_7														0			1	
CLOCK-ADD														0			1	
HORZ. CLOCK															1		0	
HORZ. RESET															1		0	
HORZ.															0			0
CAL. PROM CLOCK															1		0	
EXT. GAIN 3 lines															1			1
VERT.																0		0
SLECT BITS																1		1
CLEAR REG. D																1	0	
CLOCK REG. ABD																1	0	
61																1	0	
SO																1	0	
SERIAL																0		0
LOAD REG. A																1	0	
CLEAR REG. B																1	0	
LOAD REG. B																1	0	
CLOCK ENABLE																	1	1
BLANK																	0	0
T. F. P	0			0														

1 = INPUT, 0 = OUTPUT

*JUMPER ON MOTHER BOARD

Figure 17. Interfacing chart for Cards 1-9. Connectors A and B (22 pins each) represent external connections to and outputs from the mother board which serves to interface Cards 1-9. Thus, all connections except those of A and B are internal within the mother board and Cards 1-9 which plug into terminals on the mother board.

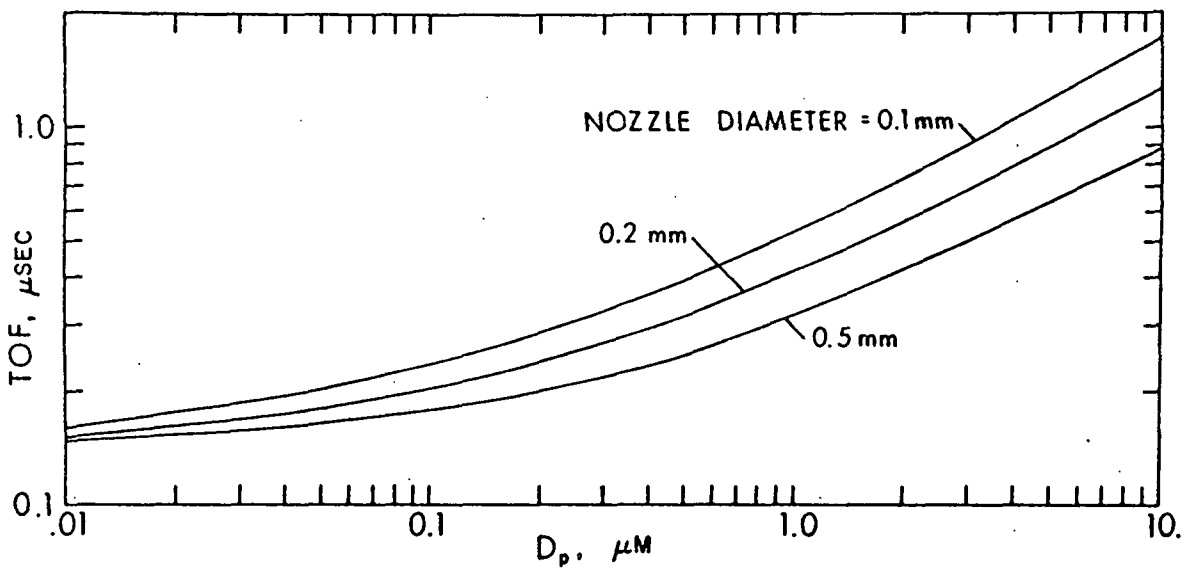

Figure 18. Calculated calibration curves for nozzle 2 of Fig. 1 with three nozzle diameters. Particle TOF was calculated for a flight path of 100 μm beginning 2 mm from the nozzle exit. An aerosol at NTP containing unit density spheres was assumed expanded through the nozzle to generate the beam.

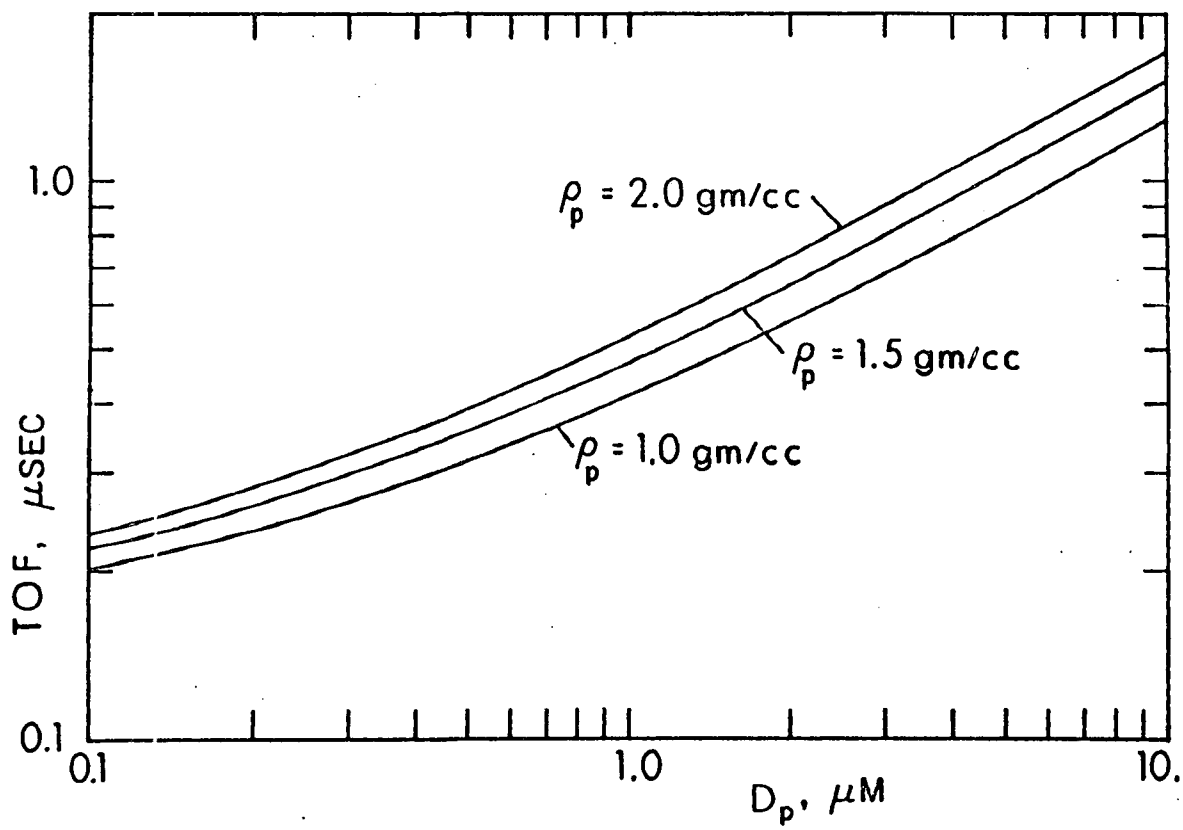

Figure 19. Calculated calibration curves for nozzle 2 of Fig. 1 for assumed expansion of air aerosols at NTP containing spheres of three mass densities. The aerodynamic diameter as it is usually defined is proportional to mass density to the 1/2 power. The mass density dependence calculated here is slightly stronger. Particle TOF was calculated for a flight path of 100 μm beginning 2 mm from the nozzle exit plane.

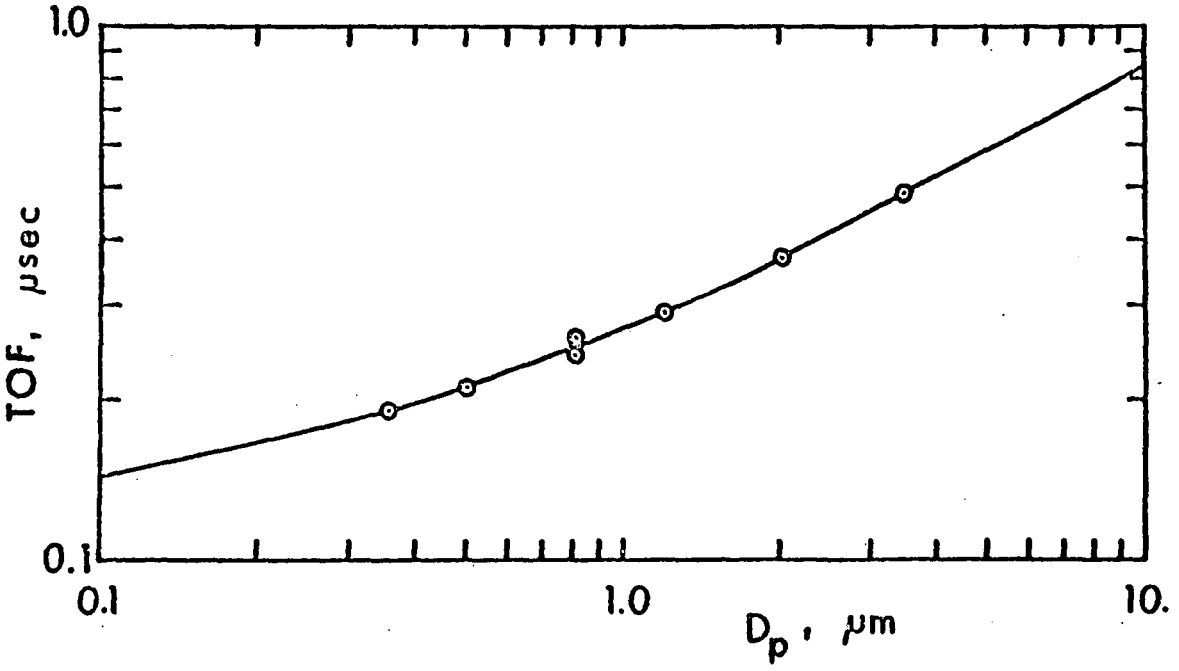

Figure 20. Comparison of calculated and measured TOF for unit density spheres assuming a light beam thickness of 72 μm.

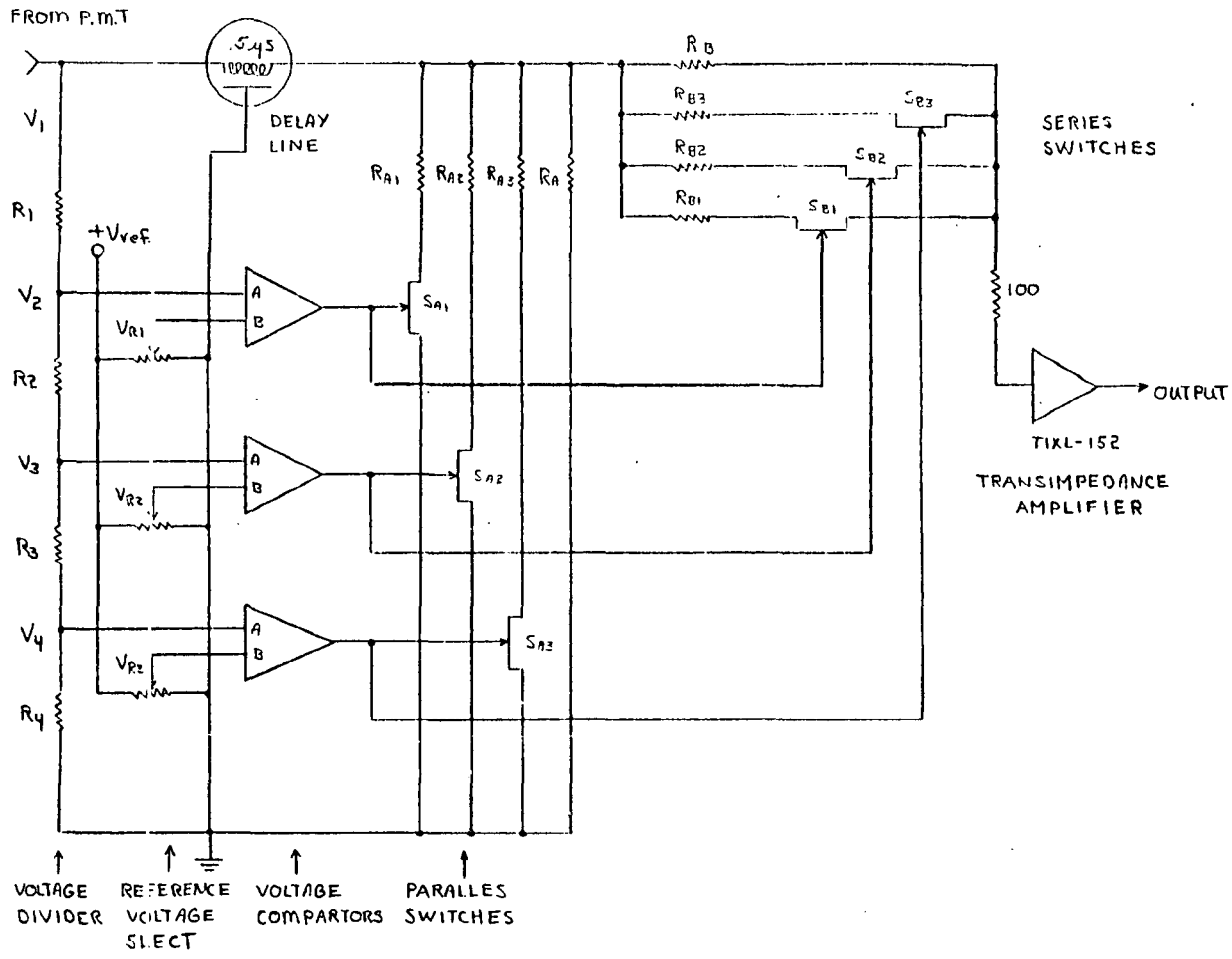

Figure 21. Example pulse compressor circuit. The PMT current pulse, delayed 0.5 μsec or longer, is attenuated by variable amounts to maintain the amplifier input signal within a limited range. This prevents amplifier chopping of large amplitude pulses. The various resistor values are selected to provide (a) the desired attenuation levels and (b) the proper output impedance for the delay line. This pulse compressor would also be useful in other systems such as in measuring scattered light signals from aerosol particles. Logic signals from the various analog comparators give the order of magnitude of the signal while the compressed pulse can easily be measured without amplifier distortion to give the pulse magnitude within the order of magnitude range (sequential coarse scale, fine scale measurement).

APPENDIX A

Reprint of a Technical Article
Entitled "Aerosol Beams".

AEROSOL BEAMS

Barton Dahneke
Radiation Biology and Biophysics
University of Rochester
Rochester, New York 14642

ABSTRACT

Because of their ability to focus large numbers of airborne particulates into a narrow beam in which the particles are isolated in a vacuum environment, aerosol beams are useful for a variety of applications in the detection and measurement of airborne particulates, in measuring particle-surface interactions and in measuring the aerodynamic and other properties of particles. Properties and applications of aerosol beams are described and critically discussed with particular interest in the use of aerosol beam techniques and devices for measuring the size distribution and other properties of airborne particulates. One aerosol beam device for measuring the particle size distribution is described in detail.

To appear in Proceedings of the Symposium on Aerosol Science and Technology, John Wiley & Sons, New York (in press).

1. Introduction

An aerosol beam is generated when an aerosol expands through an orifice, capillary or nozzle into an evacuated chamber. The gaseous portion of the aerosol jet so formed is scattered by collisions with background gas molecules and removed by pumping. The particles or droplets in the aerosol, because of their relatively large momentum, are not scattered by the background gas but form a high speed beam of the aerosol particles. The aerosol particles are thus isolated from their suspending gas, except for the background gas in the vacuum chamber, the density of which can be made very low by passing the beam through multiple pumping chambers. The particles can therefore be detected, counted, measured and collected with minimal interference from a suspending gas. These features of aerosol beams make them uniquely attractive for certain measurement techniques.

Although aerosol beams have features in common with molecular beams, these two types of beams also possess substantial differences. One example is the pumping speed required in the two systems. Molecular beams are significantly dissipated over path lengths of the order of several mean-free-paths of the background gas, due to collisions with these gas molecules. Molecular beam systems are therefore generally operated under high vacuum requiring beam skimming and several pumping chambers with relatively large vacuum pumps. Aerosol beams, because of the large momentum of the beam particles, are not rapidly dissipated in chambers of relatively high pressure. Some aerosol beam systems operated at background chamber pressures between 0.1 and 1 Torr have useful beam lengths of several cm. Such aerosol beam systems require vacuum pumps of modest size so that portable systems are possible.

To determine whether an aerosol beam technique is suitable for a particular application, the various properties of aerosol beam systems must be understood, preferably by means of accurate theories and specific experimental data or, when these are not available, by use of qualitative results and approximate information. The properties and certain applications of aerosol beams have been investigated in various laboratories. The results of these investigations are summarized and critically discussed in the next section. Later sections deal with the fundamental properties of aerosol beams, in particular with the calculation of particle velocities obtained in a beam considering the influence of nozzle shape and size, and with various applications of aerosol

beams.

2. Summary of the Properties of Aerosol Beams

2.1 Particle velocities in an aerosol beam.

Particles and droplets in an aerosol beam obtain maximum velocities in the vacuum chamber of the order of the sonic velocity of the suspending gas (1-4). Thus, particles suspended in air obtain velocities of the order of 300 m/sec while particles in helium obtain velocities of the order of 600 m/sec. The maximum particle velocity depends substantially on the particle size, mass and shape. Particles of larger size (mass) obtain lower velocities. Because of the importance of the velocity characteristics of aerosol beams, this subject will be treated in a separate section.

Limited evidence (1) suggests variation in orientation of non-spherical particles does not cause significant variation in maximum velocity. Identical particles neutrally buoyant with respect to orientation seem to obtain a unique maximum velocity due to time averaging of the influence of orientation during the acceleration process. (This topic, however, needs further investigation.) Identical particles having a preferred orientation in the accelerating jet obtain a unique terminal velocity corresponding to that preferred orientation.

2.2 Cross-section of an aerosol beam.

The cross-section of an aerosol beam always grows with downbeam displacement in the vacuum chamber. The beam divergence is, of course, caused by radial expansion of the aerosol jet as it enters the vacuum chamber. Since smaller (less massive) particles follow the gas motion more readily than larger ones, the solid angle of an aerosol beam increases substantially as the size (mass) of the beam particles decreases. Effective techniques for reducing the beam solid angle have been demonstrated. One method (5) accelerates the particles in a converging nozzle so that the particles at larger radial positions obtain larger inward radial velocity components. Upon outward radial expansion of the aerosol in the vacuum chamber, the inward radial velocity components compensate the outward components to cause a substantial decrease in the beam solid angle. A second method (6) restricts the sample particles to the central core of the gas jet and thus reduces beam solid angle by reducing the radial gas velocities seen by the particles in the expanding jet.

Collimation has been used to give extremely narrow beams. Disadvantages

of this method include biasing of the size distribution in the beam sample and plugging of the collimating hole if the aerosol sample contains a liquid fraction. Los Angeles smog plugs collimating holes rather quickly. A collimating hole in a heated plate would reduce the problem of plugging.

Because of the relationship of beam cross-section and velocity, the cross-section of uncollimated aerosol beams will be discussed with beam velocity in a separate section.

It seems possible to focus beams in one dimension by means of a gas cross-jet intersecting the aerosol beam in the vacuum chamber. Deflection of beams by asymmetric jet expansion has been demonstrated (6,7). In the similar case of a cross-jet, particles nearer to the jet source obtain larger deflections because the jet gas is more dense and better able to influence the particle motion. An aerosol beam thus deflected should obtain a relatively narrow focus. The "spot size" and focal length will depend on particle size. Two cross-jets could provide two-dimensional focusing. Such a focusing process has been independently proposed for molecular beams by Gspann and Vollman (8) and for aerosol beams by the present author. However, the technique has not yet been demonstrated for aerosols either experimentally or theoretically.

2.3 Size separation of particles in an aerosol beam.

Two techniques have been demonstrated for size separation of particles and droplets in an aerosol beam. In one (6), the aerosol beam is deflected by means of a cross-jet or by asymmetrical expansion of the aerosol jet into the vacuum chamber. Since smaller particles are more readily deflected, the particle trajectory is diverted increasingly as particle size is decreased. Upon passing through the cross-jet or asymmetric expansion region the various particle trajectories, corresponding to different particle sizes, are linear. This technique has been patented (7).

In a second method (1,4,9), particle size is discriminated by measuring particle velocity in the vacuum chamber. Since terminal particle velocity in the vacuum chamber depends on particle aerodynamic size (which will be defined in the next section), with smaller particles obtaining higher velocities, the velocity measurement or, equivalently, the measured time of flight (TOF) required for the particle to traverse a fixed path length infers the particle's size. This method of measuring particle size is also patented (7).

A technique commonly used in molecular beams can, of course, be used to

separate particles of selected velocity range, i.e., of selected size range. Velocity selectors used in molecular beam systems provide velocity resolutions $\Delta V/2V$ between 5 and 25% and maximum transmission probabilities between 27 and 49% (10-29). These selectors pass some molecules at every velocity between $V - \Delta V/2$ and $V + \Delta V/2$ with maximum transmission at V and zero transmission at the two extremes. Use of such a velocity selector with an aerosol beam should provide a velocity selected beam containing up to 49% of the total particles in the beam having terminal velocity V and lesser amounts at $V \pm \delta V$, where $0 < \delta V < \Delta V/2$. Young (30,31) describes analytical inversion methods which account for this variable transmission as well as other non-idealities of velocity selectors so that the velocity distribution of the beam can be accurately obtained from intensity data for velocity selected beams. Thus, intensity data for velocity selected aerosol beams can provide the velocity distribution function of the beam particles, which infers their aerodynamic size distribution. Since the particle number and mass distributions are frequently of "intermediate" interest for calculating other distributions, velocity selected beams have the advantage of allowing direct measurement of, say, the abundance of a certain toxic chemical present in a selected aerodynamic size range of an aerosol sample. Although all elements of the velocity selector technique have been demonstrated in molecular beam research, they have not yet been successfully applied to an aerosol beam system.

Israel and Whang (32) captured aerosol beam samples on grease coated slides to determine the deposit density distribution over the radial dimension. They proposed using such data with experimental and analytical calibration curves to obtain the size distribution of the beam particles from deposits on a coated target. Because the deposit is cumulative rather than size sorted as in (6), the analysis requires substantial microscopic counting.

The possibility of charging the beam particles and separating them in an electrostatic or magnetic field is suggested by simple analogy with mass spectrometry. However, unlike deflection of ions in mass spectrometry where one or two charges is adequate and unit charge differences are easily distinguished, aerosol beam particles require many charges to obtain adequate deflections and techniques for obtaining uniform charges of this level have not yet been demonstrated. The topic of charging of aerosol beam particles will be discussed in a separate sub-section below.

2.4 Detection and measurement of aerosol beam particles.

The most important current problem in aerosol beam technology is the development of adequate techniques for detecting and measuring particles in the beam smaller than ~0.1 μm. Detection and measurement techniques for particles ~0.1 μm and larger, such as light scattering techniques, have been demonstrated (33), some of which can also be used in aerosol beam systems. Because aerosol beam particles are isolated from their suspending gas, which frequently causes the lower detection limit in light scattering techniques, it should be possible to extend the detection and measurement limit to smaller particle sizes in an aerosol beam instrument.

Note that in order to measure the aerodynamic size of a beam particle it is sufficient in two techniques described above to simply detect the particle as it either passes a location corresponding to a deflected trajectory or as it passes two points of known separation. The problem of measuring particle aerodynamic size thus reduces to the simpler problem of detecting the presence of the particle.

One method of detecting particles in an aerosol beam has been the use of focused laser beams through which the aerosol beam is directed (1-4). The light scattered by a particle passing through the beam is directed to a photomultiplier tube (PMT) which provides a current pulse in response to the scattered light signal. One instrument (4) using this method can measure particles of 0.3 μm diameter and larger. With simple changes, their capability can be extended to ~0.1 μm, but this limit is still inadequate. Moreover, the laser system and associated electronics are large and expensive.

An alternative technique has been proposed by Schwartz and Andres (9), wherein beam particles pass through a velocity selector before they are accumulated on a peizo-electric crystal surface where their mass is measured by observing the change in the frequency of oscillation of the crystal. However, this method may not be practical because unless the crystal surface is coated to prevent particle bouncing, the particles are not retained on the crystal surface. On the other hand, if the crystal is coated with, say, a layer of grease sufficiently thick to capture particles, the mass loading may already be so high that the crystal operates in the non-linear range so that frequency changes cannot be used to monitor adsorbed mass changes.

Holländer and Schörmann (34) demonstrated a novel technique wherein aerosol beam particles were impacted on a thin plastic membrane which had been

reflective coated and was one of the mirrors in an interferometer. By observation of the interference patterns (momentum changes) and independent measurment of particle velocities they could measure particle mass directly, to a lower limit of 10^{-12} gm (1.3 μ particle diameter for a unit density sphere). The system was large, complex and expensive and only suited for laboratory measurements.

The interferometer technique just described recalls an earlier technique of Avy and Benarie (35) described in one of the first papers on aerosol beams. In their instrument Avy and Benarie directed an aerosol beam towards a sensitive microphone. The instrument was able to detect particles above 30 μm diameter. A refined instrument was described by Benarie and Quetier (36). With it the authors could monitor the mass loadings of particles between 1 and 20 μm diameter.

Hepburn, et al., (37,38) detected beams of highly charged glycerol droplets by impacting them onto a phosphor screen or liquid crystal target. The resulting luminescence of the phosphor screen revealed the beam geometry and density distribution. Although this method removes the particles from the beam when they strike the screen, this detection technique may be useful with aerodynamic deflection in measuring the size distribution of the beam particles.

A technique for measuring the quantity of any of various atomic and molecular species present in individual beam particles or in accumulated samples has been described by Myers and Fite (39) and by Davis (40). The technique comprises impaction of the beam particles onto a heated filament, usually rhenium at about 1200°C, where the particles apparently stick and evaporate. The evaporating atoms or molecules having sufficiently low ionization potential are ionized by the rhenium filament, because of its high work function. The ions thus generated are focused into a quadrupole mass filter or magnetic analyzer whereby the quantity of ions of a selected charge to mass ratio can be monitored. Some of the compounds which Davis was able to observe using this technique are listed in Table 1.

Because of the difficulty in detecting small particles in aerosol beam systems, it is sometimes desirable to grow the particles to a larger size by condensation of a supersaturated vapor. The larger particles can be easily detected by, say, scattered light signals. Although the initial size distribution of the particles is not determined, this type of absolutely calibrated

condensation nuclei counter (CNC) can detect each particle present which is larger than the critical cutoff diameter (~20 Å) and wettable by the condensing vapor. (The importance of the latter condition seems to be poorly understood.) Use of this CNC with additional devices that discriminate particle size, such as an impactor, filter or diffusion battery, would allow inference of the original size distribution of the aerosol sample. Further details of this proposed system are discussed in (4).

2.5 Particle bouncing and sample collection.

Both experiments (41,42,43) and theory (44) have demonstrated that micron size solid particles striking solid surfaces will bounce when the normal component of their incident velocity exceeds ~1 m/sec. Viscous droplets are captured on target surfaces placed in high velocity aerosol beams; however, they burst upon impact so that parts may be lost from the target surface. Solid particles are captured when the target surface is coated with a viscous layer to dissipate the kinetic energy of the incident particle.

These results indicate that samples of aerosol beam particles should be collected on grease coated targets or in special collectors within which the particles will rebound many times without escaping. An exception appears to be sampling on a heated filament. Evidently the particle tip is melted on contact so that it provides its own viscous layer.

The grease coating on a collector surface must be supplemented or replaced periodically to prevent a solid overcoating on the grease surface. This can readily occur in highly focused aerosol beams of solid particles.

Because solid particles moving at typical beam velocities may bounce on uncoated solid surfaces many times before being captured, particles reflected from, say, a velocity selector will reflect throughout the vacuum chamber. Care must be taken to prevent "background particles" from reaching the detection system.

2.6 Alteration of particles in an aerosol beam.

Possible mechanisms by which sample particles may be altered in an aerosol beam include evaporation, condensation, cooling in the adiabatically expanding jet, freezing, breaking of frozen particles, breaking of droplets and aggregates during acceleration and charging of particles in the accelerating flow. The importance of the last four mechanisms in aerosol beam systems is not well understood. These topics need investigation. The first

three, on the other hand, have been investigated.

In the course of measuring the free molecule drag on latex beam particles passing through a deceleration chamber containing dilute air at controlled pressure, one group of investigators (2,3) found the spheres had different drag coefficients when the beam was accelerated in an air jet (air aerosol) or in a helium jet (helium aerosol). The data and the associated analysis of these authors suggest the difference is due to cooling of the latex spheres in the adiabatically expanding jets, with substantially more cooling occurring in the air jet. The authors estimated 2.02 μm latex spheres were cooled some 30°C in the air jet expansion but only a few degrees in the helium jet. The difference seems to be due to condensation of gas molecules in the air jet which draw their latent heat of evaporation from the warmer particles thus causing significant cooling of the particles in the air jet. In the helium jet no condensation was expected at the given expansion ratio so that these particles were apparently not cooled by cluster evaporation.

The authors (2) went on to estimate the evaporation loss of a 1 μm water droplet in an aerosol beam taking into consideration the cooling of the droplet in the air jet expansion process and the cooling of the droplet by evaporation. They estimated that the droplet diameter would decrease by less than 3% over intervals of ~1 msec, i.e., sufficient time for a particle flight of 40 cm in the vacuum chamber. Thus, evaporation of droplets does not appear to cause substantial alteration of aerosol beam particles.

Another investigation (4) has shown that condensation in the jet does not significantly alter beam particle size, even for high inlet vapor pressures, because the rapidly accelerating particles spend too little time in the supersaturated region of the jet to realize significant growth. This topic will be discussed further in the next section.

In the case where a thin surface layer of liquid or adsorbed vapor is of interest, then evaporation and condensation can have substantial effect in altering particles in the beam.

2.7 Electric charging of aerosol beam particles.

Because of its relation to the detection and measurement of particles in an aerosol beam, this topic is of substantial interest. Unfortunately, its importance has not been fully appreciated and relatively little work has been done.

Aerosol beams of charged particles can be obtained in several ways. First, the particles can be generated in a manner that causes them to have a high charge level (45) or the aerosol can simply be passed through a suitable charging device (46) before it enters the aerosol beam system. Second, the particles or droplets may be charged by breaking up in the air stream during their acceleration in the jet, as mentioned earlier. Although this topic has been investigated over many years in connection with meteorological studies (47) (the generation of charge in thunderclouds) it is not yet well understood.

A third way of obtaining a beam of charged particles is by charging the particles by means of a crossed electron beam in the vacuum chamber. This technique takes advantage of the vacuum environment of the beam particles, as the electron beam would be dissipated too quickly except at sufficiently low gas density. Hall and Beeman (48) have demonstrated the charging of polystyrene latex beam particles in a sheet electron beam of 4 to 10 mA current with electron energies of the order of 100 eV. The beam particles required between 5 and 10 μsec to traverse the electron beam during which time they experienced an (overestimated) surface temperature increase of 17°C. Latex particles of 0.357 μm diameter obtained a calculated charge of 620 electronic charges while 0.557 μm particles obtained 965 charges.

A similar process, namely the charging of clusters in molecular beams, has been discussed by Hagena (49). Dolder (50) reviews several techniques and results of molecular beam investigations of ionization processes and interactions of charged and neutral particles. Some of the techniques he describes may be useful in aerosol beam systems.

Charging of beam particles is an important problem which deserves further investigation. This topic is discussed further in the applications section.

2.8 Coincidence errors in particle counting.

In the counting or measurement of aerosols of high number concentrations, coincidence errors due to simultaneous occupation of an "observation volume", such as a focused laser beam, by more than one particle can become substantial. We show here that such problems are less serious in aerosol beam systems.

Consider a system in which the aerosol particle flow rate is $N_i A_i V_i$, where N_i is the particle number concentration, A_i the flow cross-section and V_i the average particle velocity at location i. From conservation of particles

$$N_2 A_2 V_2 = N_1 A_1 V_1 .$$

Assuming negligible particle loss to the system walls, this expression must apply regardless of whether the aerosol particles are suspended in a gas medium or a vacuum.

The linear density $N_i A_i$ (particles/cm) provides a measure of the probability of a coincidence error occurring within the observation volume of fixed thickness L. That is, for more particles per cm in the stream the probability that more than one occupies the interval L at any time must increase. Because the linear density

$$N_2 A_2 = N_1 A_1 V_1 / V_2$$

is smaller in an aerosol beam where V_1/V_2 is small, coincidence errors in aerosol beam systems are always less than in other systems where V_1/V_2 is larger.

Thus, for a given coincidence error level, it is possible to count or measure sample particles at higher number densities in an aerosol beam system than in other systems.

3. Calculation of the Dynamical Properties of Aerosol Beams

The fundamental properties of aerosol beams most pertinent to their evaluation as possible experimental or industrial systems are the velocity and geometry characteristics of such beams. This section reviews methods for calculating these properties of aerosol beams and presents example results. A related problem of fundamental interest, namely, condensational growth of particles in adiabatically expanding jets, is also considered.

The motion of an aerosol particle in a fluid stream is described by the particle equation of motion

$$m_p \frac{d\vec{v}_p}{dt} = - [f + \frac{dm_p}{dt}](\vec{v}_p - \vec{v}_f) \qquad (1)$$

where m_p is the particle mass (which may change with time due to evaporation or condensation), $\vec{v}_p$ the particle velocity, t the time, f the particle friction coefficient and v_f the local fluid velocity. The ratio $\alpha = f/m_p$ is given by

$$\alpha = 9\mu\kappa/2a^2\rho_p C_s \qquad (2)$$

where μ is the local gas viscosity, a the particle radius (or equivalent

sphere radius), ρ_p the particle mass density, C_s the slip correction factor and κ the dynamic shape factor that includes two factors $\kappa = \delta\sigma$ that correct for non-negligible particle Reynolds number and for non-spherical particle shape. Example corrections for non-spherical shape σ, as well as the values of C_s for such shapes, are described for several geometries by Dahneke (3,51, 52). The factor δ is given for spheres by the empirical expression

$$\delta = 1 + 0.1062\ Re^{0.8561} \tag{3}$$

where

$$Re = 2a\rho_f\ |\vec{v}_p - \vec{v}_f|/\mu,$$

ρ_f being the local mass density of the fluid. This expression for δ was obtained by fitting the coefficient and exponent to experimental data for spheres in continuum flow (53,54) to provide an adequate approximation when $Re < 50$, which is the Re range encountered in aerosol beam generation.

For aerosol expansions through nozzles, orifices and capillaries of circular cross-section, the vector equation (1) is equivalently expressed in two scalar equations for the axial (z) and radial (r) components of particle motion. Thus,

$$m_p \frac{dv_{pz}}{dt} = -\left[f + \frac{dm_p}{dt}\right](v_{pz} - v_{fz}) \tag{1a}$$

$$m_p \frac{dv_{pr}}{dt} = -\left[f + \frac{dm_p}{dt}\right](v_{pr} - v_{fr}). \tag{1b}$$

If we define

$$\alpha'(t) = \left[f + \frac{dm_p}{dt}\right]/m_p,$$

then the solutions of these equations are

$$v_{pz}(t) = e^{-\int_o^t \alpha' d\nu}\left\{v_{fz}(o) + \int_o^t e^{\int_o^\theta \alpha' d\nu}\, v_{fz}(\theta)\alpha'(\theta)d\theta\right\} \tag{4a}$$

$$v_{pr}(t) = e^{-\int_o^t \alpha' d\nu} \left\{ v_{fr}(o) + \int_o^t e^{\int_o^\theta \alpha' d\nu} v_{fr}(\theta)\alpha'(\theta)d\theta \right\} \tag{4b}$$

and

$$z(t) = z(o) + \int_o^t v_{pz}(t)dt \tag{5a}$$

$$r(t) = r(o) + \int_o^t v_{pr}(t)dt. \tag{5b}$$

These equations form the basis of numerical programs for tracing the motion of particles in accelerating jet flows. When evaporation or condensation has significant influence on particle motion or is otherwise of interest, an energy equation coupled to the equation of motion may also need to be solved simultaneously.

When evaporation or condensation does not have significant influence on particle motion, the $\alpha'(t)$ in equation (4) can be replaced by the α of equation (2). In this case it is sometimes convenient to delete the intermediate parameter t from the calculation by use of the chain rule.

$$v_{pz} \frac{dv_{pz}}{dz} = -\alpha(v_{pz} - v_{fz}) \tag{6a}$$

$$v_{pr} \frac{dv_{pr}}{dr} = -\alpha(v_{pr} - v_{fr}) \tag{6b}$$

Although these expressions are non-linear which tends to make their numerical evaluation unstable, they are sometimes very convenient.

For example, when aerosol beams are decelerated in a motionless background gas, their dynamics is especially simple since $\vec{v}_f \equiv 0$. For this case axial motion of the beam particles is described by the simple expression

$$v_{pz} = \int_{z_s=0}^{z_s} \alpha(\nu)d\nu \tag{7}$$

where z_s is the upbeam distance from the particle's stopping location with a similar expression applying for radial particle motion. For sufficiently small z_s, (7) simplifies to

$$v_{pz} = \alpha z_s \tag{7a}$$

where α is the constant given by expression (2). Dahneke and Friedlander (55) and Dahneke (2,3) verified expressions (7) and (7a) for aerosol beams in a motionless background gas and Dahneke (41) used this property of aerosol beams to measure the capture of beam particles on target surfaces.

To calculate beam particle velocities, beam cross-sections and evaporation or condensation obtained in an aerosol beam, the fluid flow field $\vec{v}_f$ in equation (1) must be known. The temperature, pressure and density fields of the suspending gas are also required in these calculations. These present a substantial problem. Fortunately, analytical, semi-empirical and empirical expressions provide simple approximations of the gas jet centerline velocity and state properties for nozzle flows. These simple approximations can be used to estimate some of the properties of aerosol beams.

The fluid flow field in aerosol beam systems divides into four regions: the nozzle orifice or capillary entrance region, the internal flow region within the nozzle, the transonic flow region at the nozzle exit and the supersonic free jet flow region. Beyond these regions the vacuum is generally adequate so that the motion of the beam particles is not significantly influenced by the background gas except where high background pressures or long path lengths occur.

Of the four flow regions, the entrance is usually not significant in nozzle flows. It can be important in capillary flows, as discussed below. But capillaries are not advised in aerosol beam systems because of particle losses on the wall, especially in the entrance region. Thus, entrance region flow is not generally important in aerosol beam dynamics and will be discussed below only briefly in connection with capillary flows. Flow in the transonic region near the nozzle exit is not understood. This flow region comprises one of the classic unsolved problems of gas dynamics. Approximations of the centerline flow must therefore be based on expressions for the nozzle and free-jet regions.

The simplest model of compressible nozzle flow assumes one-dimensional,

isentropic, frictionless flow of an ideal gas. This model provides simple expressions for the gas velocity and all the properties of a gas in terms of the stagnation condition of the gas and the local area ratio A/A*, where A* is the nozzle throat area. These expressions are derived by Shapiro (56).

The Mach number M is defined by

$$M = v_f/\sqrt{RT/\mathcal{M}} \tag{8}$$

where v_f is the local gas velocity, R the universal gas constant, T the local absolute temperature of the gas and $\mathcal{M}$ the gas molecular weight. The Mach number and area ratio are related by

$$A/A^* = \left\{\left(\frac{2}{\gamma+1}\right)\left(1 + \frac{\gamma-1}{2} M^2\right)\right\}^{\frac{\gamma+1}{2\gamma-2}} \Big/ M \tag{9}$$

where γ is the ratio of specific heats: $\gamma \equiv c_p/c_v = 7/5$ for air, 5.3 for helium and 9/7 for CO_2. The local state parameters of the gas are given by

$$T_o/T = 1 + (\gamma-1)M^2/2 \tag{10a}$$

$$p_o/p = (1 + (\gamma-1)M^2/2)^{\gamma/(\gamma-1)} \tag{10b}$$

$$\rho_o/\rho = (1 + (\gamma-1)M^2/2)^{1/(\gamma-1)} \tag{10c}$$

where T_o, p_o and ρ_o are the stagnation state properties of the gas.

The most severe of the above assumptions in the case of small nozzles is the assumption of frictionless flow. This topic will be briefly discussed below.

Free-jet flows have received considerable interest because of their use in continuum source molecular beams. The properties of these jets are therefore known. This subject has been reviewed by Ashkenas and Sherman (57), by French (58) and, more recently, by Anderson (59).

Ashkenas and Sherman give an accurate fitting for the centerline Mach number of a free-jet

$$M = AB - \frac{1}{2}\left(\frac{\gamma+1}{\gamma-1}\right)/(AB) + C/B^3; \quad B = \{x/D - x_o/D\}^{\gamma-1} \tag{11}$$

where D is the nozzle diameter and x the downstream distance from the nozzle

exit plane. For air jets $\gamma = 1.40$, $A = 3.65$, $C = 0.20$ and $x_o/D = 0.40$. These authors also provide values for other gases. This expression applies for the range

$$1.0 < x/D < 0.67\ (p_o/P_b)^{1/2},$$

the upper limit being the location of the Mach disc or normal shock where the overexpanded supersonic jet shocks to the background pressure. The ratio p_o/p_b is the ratio of stagnation to background pressure in the vacuum chamber. The third term of the fitting formula is not included by Ashkenas and Sherman on the basis of analytic considerations, as are the first two terms (by comparison to radial source flows). For the case of air and helium jets it does extend the range of validity of the two term fitting formula, the two term version being only valid above a lower limit of $x/D = 6$.

Since the gasdynamics solutions are not available for the transonic flow region near the nozzle exit, flow in this region can be approximated by a suitable expression that fits the boundary condition $M = 1.0$ at $x = 0$ and matches expression (11) when $x/D > 1$. The result for the centerline Mach number in the free jet within the range $0 < x/D < 6$ is

$$M \cong 1.0 + A'X/D - B'(x/D)^{5/2}. \qquad (12)$$

When $\gamma = 1.40$, $A' = 1.55$ and $B' = 0.042$. The form of this expression is suggested by the curves of French (58). Since the free jet flow is assumed to be isentropic flow of a perfect gas, the centerline Mach number of expressions (11) and (12) can be combined with expressions (8) and (10) to obtain the centerline gas velocity and state properties.

The assumption of frictionless flow in the nozzle-jet system causes errors in the calculated flows due to several types of viscous effects (57). The most important of these in the small nozzle system used in aerosol beam generation seems to be boundary layer formation. The boundary layer can produce a change in the effective nozzle diameter and a distortion of the flow pattern in the transonic region near the nozzle exit. The effect is reduced as the nozzle Reynolds number is increased, since boundary layer growth in the nozzle is diminished. Ashkenas and Sherman (57) present experimental data relating effective orifice size to nozzle throat Reynolds number for two orifices and one long nozzle with length/diameter ~4. Their data suggest the

influence of the boundary layer is not important for nozzle throat Reynolds number exceeding a few hundred.

These centerline flow approximations for the nozzle, transonic and free-jet flow regions appear to be generally adequate for calculating aerosol beam velocities, since it is good practice to confine the aerosol sample to the central core of the jet flow to obtain "focused" aerosol beams (6). Also, for isentropic expansions of air at NTP, the calculated nozzle throat Reynolds numbers for throat diameters of 100, 200 and 500 μm are 1470, 2490 and 7340, respectively, so that boundary layer formation should not substantially affect the flow.

Figure 1 shows a comparison of measured particle velocities and those calculated by use of the above approximation for the centerline gas flow (1). The converging nozzle used to obtain these data had a diameter of 0.40 mm, a length of 2.1 mm and was operated at a calculated nozzle throat Reynolds number of 5870. The particles were confined to the central core of the nozzle flow. A collimating orifice was located 2 mm downstream of the nozzle exit so that a normal shock must have occurred just upstream of this location, but the particles had essentially obtained their terminal velocity before reaching this plane. Particle deceleration behind such a shock was calculated to be a few percent for the smallest spheres used (0.81 μm diameter) and was less for larger sizes. The close agreement of the calculated and measured data suggests the simple expressions for the centerline gas flow are adequate.

Similar results reported by Dahneke and Padliya (4) are shown in Figure 2 for a different nozzle having a diameter of 0.2 mm, a length of 1.5 mm and a throat Reynolds number of 2940. Again, the particles were confined to the central core of the nozzle flow. The data of Figure 2 are presented as particle TOF across a fixed path length of 72 μm. This path length, the thickness of a focused laser beam, was determined by fitting the calculated TOF curve to the data. However, the close agreement of the curvature of the calculated and experimental curves again suggests the calculated particle velocities are accurate. Calculated flow values and particle velocities for this nozzle-jet system are shown in Table 2.

Figure 3 shows values of terminal particle velocities obtained in the expansion of an aerosol of latex spheres of density 1.027 (2.02 μm) and 1.05 gm/cm^3 (otherwise) in air and helium jets. These jets were generated by

expansion of the aerosol at NTP through a capillary with square ends, a length of 300 mm and diameter of 0.50 mm. The aerosol beam was collimated so that the velocities correspond to centerline flow. This collimating effect tends to occur naturally in long capillaries anyway, because the Bernoulli force acting on the particles in the parabolic velocity field causes them to concentrate in the center of the capillary. The data have not been compared to calculated velocities because no simple theory is available for choked capillary flow (60). The largest particles obviously do not obtain velocity equilibrium with the expanding helium jet at the capillary exit. Expressions (11) and (12) for the centerline Mach number are probably inadequate in free-jet flows originating from a capillary because the flow in the capillary is a boundary layer flow.

Figures 4-6 show calculated particle TOF across a 100 μm path length beginning 2.0 mm from the nozzle exit plane for spherical particles of unit mass density. Nozzle 1 of Figure 4 is the nozzle for which the data of Figure 2 were measured and calculated, except for a constant diameter section of 0.1 mm length at the outlet end not present in nozzle 1. Comparison of the three calculated curves show that nozzle geometry does not have substantial influence on particle terminal velocity.

Substantially larger differences in particle terminal velocity occur with changes in nozzle diameter, as shown in Figure 5. This happens because the nozzle and free-jet flow fields are scaled to the nozzle diameter. A larger nozzle diameter means a slower rate of increase in gas velocity over (unscaled) axial distance so that the accelerating particles can follow the gas motion more closely. That is, particles in a larger diameter jet lag the gas velocity less than in a smaller jet. Particles in a smaller jet therefore have larger TOF as shown in Figure 5.

This feature becomes important in certain applications of aerosol beams such as in a time of flight aerosol beam spectrometer (TOFABS) (1,4). As illustrated by the curves of Figure 5, to retain size resolving power down to small particle sizes it is important to use a small diameter nozzle, which is also helpful in reducing vacuum pumping requirements. The improvement thus obtainable in small particle resolving power greatly exceeds the improvement obtainable by shortening the nozzle or otherwise changing its geometry.

Although the above conclusion is believed to be generally valid, it

should be noted that the calculated particle TOF values for the conical section nozzles of Figures 4-6 may be less accurate than the calculated values of Figures 1 and 2. Since the flow is actually converging rather than parallel at the exit of these conical section nozzles, the effective value of nozzle diameter D and apparent origin location x_o in expressions (11) and (12) may be slightly different. No accurate beam velocity measurements have yet been reported for conical section nozzles or any nozzles not having a constant diameter length at the nozzle exit.

Figure 6 shows the influence of particle mass density on particle TOF for nozzle 2 of Figure 4. Particles of unknown mass density can only be characterized in terms of their aerodynamic diameter, which is defined as the geometric diameter of a sphere of reference mass density obtaining the same TOF. Since atmospheric particles and droplets often have average mass densities near 1.8 gm/cm^3, a reference density of 1.8 gm/cm^3 would be useful for defining the aerodynamic diameter of atmospheric particles as this would give an aerodynamic diameter corresponding closely to the particles' geometric diameter.

Dahneke and Padliya (4) used the simple centerline flow theory, expressions (8) through (12), together with an interpolation formula for the condensational growth of small particles in an adiabatically expanding jet. Their interest in this problem was in the possible use of condensational growth to aid in the detection of very small particles. They therefore considered jet expansions containing various vapors added to the aerosol sample at their saturation pressure for this purpose. Although some questionable assumptions were made in the calculations, such as assuming temperature equilibrium between the particle (droplet) and expanding gas throughout the nozzle flow, these assumptions were conservative in the sense that they would cause an overestimate of condensational growth. Thus, actual growth would be less than their calculated results shown in Table 3. The calculations reveal that increase in particle size is not significant in the jet because the particles spend insufficient time in the growth region between the critical supersaturations for the onset of heterogeneous nucleation and homogeneous nucleation. Dahneke and Padliya concluded that to obtain sufficient growth to aid particle detection, the particles must be allowed to grow in a growth chamber upstream of the jet in which the vapor supersaturation is controlled by, say, a relatively small pre-expansion of the gas-vapor-sample mixture.

Of course, the centerline gas velocity and properties cannot be used to calculate aerosol beam expansions in the vacuum chamber. The calculations of Israel and Whang (32) and the measured data of various investigators (5,6,32) remain the only information available. Some aerosol beam diameters measured by the present author are shown in Figure 7.

Israel and Whang (32) analyzed the dynamics of aerosol beams generated by aerosol expansion through a capillary and converging nozzle and compared their results to experimental data. They considered three flow regions: flow near the capillary or nozzle inlet, flow within the capillary or nozzle and free jet expansion flow near the capillary exit. In each case they made idealized assumptions to simplify the calculations. However, their calculated results reveal interesting details of the beam dynamics which were supported by their measured data.

For expansion flows through a capillary, they found that the beam geometry in the vacuum chamber was substantially influenced by the entrance region flow. They predicted and observed annular deposits reminiscent of the "halo deposits" sometimes observed in impactor samples. Such deposits were also reported for capillary expansions in one figure of Israel and Friedlander (5). Israel and Whang's analysis indicates this effect in aerosol beams (and probably in impactors) is due to the particle distribution in the flow field obtained in the inlet flow region of the capillary and to the beam expansion caused by the radial expansion of the jet in the vacuum chamber. In their converging nozzle design this effect was not significant.

To analyze the beam dynamics for the converging nozzle expansion, they assumed parallel sonic gas velocity at the nozzle exit plane and velocity equilibrium between the gas and the suspended particles. Beam dynamics in the vacuum chamber other than parallel, constant velocity motion were therefore assumed caused by the free jet expansion. Furthermore, they assumed the free jet flow was adequately characterized by planar, two dimensional flow as would occur in the central region of a long, narrow slit nozzle. They solved for this two-dimensional flow field using the method of characteristics.

Israel and Whang calculated the particle trajectories in the calculated flow field to obtain beam diameter (radial expansion) versus downbeam distance for various aerosol particle sizes and compared these results to their measured data. The data generally supported the calculated results. Israel and Whang's

investigation, besides providing interesting details, suggests the general result that the dynamics of aerosol beams of submicron particles generated in long slender nozzles are predominantly due to the acceleration of the beam particles in the free jet expansion. This conclusion is also suggested by the results obtained using much shorter nozzles in the present author's laboratory, provided the beam particles are $\lesssim$ 0.1 μm diameter. For larger particles a substantial velocity difference can occur between the particles and gas so that beam dynamics are strongly influenced by flow in both the nozzle and free-jet regions, as shown in Table 2.

Since the above investigations, several techniques have been reported which provide improved estimates of the flow properties in nozzles, orifices and capillaries. These techniques have been recently reviewed by Edwards (60). Although a general solution of the Navier-Stokes equations for compressible flow in a capillary, orifice or nozzle has not yet been reported, experimental investigations and model calculations have provided considerable information about these flow systems. None of these data or techniques have yet been applied in aerosol beam calculations.

4. Applications of Aerosol Beams

Aerosol beams have been used in several applications and proposed for others. Examples include systems for the size sorting of fine powders (1), for measuring particle drag (3), particle bounce and particle adhesion energy (41,42), particle size or mass distributions (1,4,9,32,34-36), composition of particles (39,40) and the electrical charging of particles (37,38,45,48). All of the systems used in these investigations were experimental in the sense that they attempted to incorporate a new technique for which little precise information was available into a system capable of accurate measurements. For this reason alone, the results of each of these investigations are useful because, in addition to demonstrating the advantages and limitations of the various applications, they provide useful information about the properties of aerosol beams.

One application of aerosol beams, namely, time of flight aerosol beam spectrometry (TOFABS) (1,4,7,9) will be described in detail. Although this particular application was rather arbitrarily selected, it comprises an important application and illustrates some of the unique features of aerosol beams. It also illustrates an important current need in aerosol beam

technology, namely, the development of adequate techniques for detecting and measuring small particles in the beam.

TOFABS instruments can be used for measuring the size distribution of airborne particles. This type of instrument infers a particle's aerodynamic size by measuring its TOF in the vacuum chamber, as described previously. Example results from Reference (1) showing the capability of this technique are shown in Figure 8. These data show the number of particles counted versus particle TOF between two focused laser beams of 1.077 cm separation. The aerosol samples measured were monodisperse latex spheres and aggregates (doublets, triplets, etc.). Two sample aerosols were separately measured containing spheres of 1.25 μm diameter (solid curve) and 2.02 μm diameter (dashed curve), respectively. The aerodynamic size difference between the singlet spheres and doublet aggregates in air at NTP is 19%. The TOFABS easily resolves differences of this magnitude and seems capable of resolving smaller differences.

Because of the relatively large separation of the light beams in the above apparatus, the particle TOF values were large. This had the consequence that only rather dilute aerosols could be measured. For aerosol number densities > 10^3 particles/cm^3 coincidence counting errors would have become significant.

To solve this problem the single beam TOFABS of Figure 9 was built. In this version, the vertical downward aerosol beam intersects a single horizontal laser beam at its focus. As each beam particle passes through the laser beam, it scatters light into the spherical mirror which focuses the scattered light signal onto a small deflector mirror which directs the signal onto a photomultiplier tube (PMT). The instantaneous amplitude of the PMT signal therefore corresponds to the instantaneous location of the particle in the laser beam.

Because the intensity distribution in the laser beam was Gaussian, the PMT signals were Gaussian in time as the particles traversed the laser beam at constant velocity, provided the particles were small compared to the laser beam thickness of 72 μm. Such Gaussian signals are shown for monodisperse latex spheres of 2.02 μm diameter as the upper oscilloscope trace of Figure 10. The lower trace is a logic pulse of constant amplitude and of width equal to the particle TOF across the laser beam. This logic pulse was provided by the circuitry shown in Figure 11, which assured that the particle TOF was

always measured for a fixed path length.

Figure 2 shows experimental calibration data obtained using latex spheres, compared to an analytical calibration curve fitted to the data by selecting the laser beam thickness giving the best agreement (72 μm).

An example size distribution measured with this instrument is shown in Figure 12. The sample was a heterodisperse NaCl aerosol obtained by spraying an aqueous solution in air and allowing the droplets to dry. The vertical axis is number of particles measured while the horizontal axis is TOF (particle aerodynamic size). The maximum in the distribution curve occurred at 0.9 μm diameter.

This TOFABS can measure particles between 0.3 and about 10 μm diameter. The lower size limit occurs because the scattered light signals are sufficiently weak for smaller particles so that statistical or "shot" noise, due to statistical fluctuations in the small number of photons reaching the PMT, prevents accurate measurement of the instantaneous location of smaller particles in the laser beam.

Because of substantial interest in particles of smaller size (the "respirable" size range covers particle diameters between a few hundredths to a few μm) current research in the author's laboratory is investigating methods for detecting beam particles of small size and thereby extending the measurable size range of TOFABS instruments. Since these particles can be isolated from their suspending gas, very sensitive detection techniques capable of sensing particles much smaller than 0.1 μm should be usable in detecting small particles without removing them from the beam or attenuating their velocity.

One promising detection technique is electron beam scattering. The following analysis of the scattering of an electron beam by charged aerosol beam particles illustrates the important features of the process and suggests that particle detection by this technique should be possible. The complete analysis is too complex to summarize here. Only the simplest prototype problem will be considered. However, this prototype problem shows all the important features of the scattering process and provides an order of magnitude approximation of the attainable signal level. A more complete analysis will be described elsewhere.

Consider an aerosol beam passing through a crossed electron beam which charges the beam particles, as in the experiments of Hall and Beeman (48).

The design and performance of such electron beams are described in References 61-64. The aerosol beam particles, now charged, will scatter electrons in passing through other electron beams and may thereby be detected and measured. We wish to determine the magnitude of the signals obtainable by electron beam scattering and whether this detection method seems useful for small aerosol beam particles.

In order to prevent the disintegration of small droplets when the repulsion of their surface charges exceeds their surface tension, i.e., to prevent the droplet charge from exceeding the Rayleigh limit, we assume the electron beams of such a system to be low energy beams. High energy beams and detection of particles by secondary electron emission will not be considered here. Thus, the energy and current of the first electron beam is controlled so that particles obtain a desired (size dependent) saturation charge in this electron beam. They retain this same charge while passing through a subsequent beam or beams. (In fact, measurement of particle charge may also be useful in inferring the size of the aerosol beam particle.)

Rutherford (65) analyzed the deflection of a small charged particle (an electron in the present problem) by coulombic interaction with a more massive charged particle. He assumed the interaction of point charges and used conservation of angular momentum to calculate the angle ϕ by which the electron's final trajectory is deflected from its initial trajectory. He obtained

$$\cot(\phi/s) = 2\ r/b \qquad (13)$$

where r is the minimum separation between the initial electron trajectory and the charged particle. The trajectory of the more massive particle is not significantly altered by the interaction. In fact, we can regard the more massive particle as stationary.

The quantity b is given by

$$b = 2\ Ne^2/(mu^2)$$

where, for the present application, N is the number of electronic charges on the aerosol beam particle, e the unit electronic charge, m the electron mass and u the electron velocity. The quantity b represents a simple physical quantity, namely, the minimum separation of the two point charges obtained when the initial electron trajectory intersects the charged particle.

Rutherford's result for ϕ is therefore exact for charged particles of radius a provided $a \ll b$ or $r \gg a$. If one of these conditions is not satisfied the point charge assumption may no longer be adequate. We shall assume and later demonstrate that (13) is an adequate approximation in the present calculations for low energy electron beams.

Rutherford's result for ϕ applies irrespective of the sign of the charge on either particle, since the same deflection angle ϕ is obtained, albeit with opposite sign, by coulombic repulsion or attraction.

The simplest prototype problem we are considering here comprises passage of a charged particle through the center of a parallel, circular electron beam of radius R. This system, having collectors C_1 and C_2 for the scattered and unscattered electrons, is shown in Figure 13. Collector C_1, having a hole of radius $R_1 > R$ and outer radius R_1', is located an axial distance L from the scattering particle.

Electrons with initial trajectory at r will fail to intercept C_1 if their deflection angle ϕ given by (13) exceeds the angle ψ', where

$$\tan \psi' = (R_1' - r)/L.$$

That is, when

$$2 \arctan \{b/2r\} > \arctan \{(R_1' - r)/L\}.$$

Since only electrons at small r obtain sufficient deflection, this expression applies when $r \ll R_1'$. Thus, electrons will fail to strike C_1 because their deflection angle is too large when

$$r < r_o = b/\{2 \tan \tfrac{1}{2} \arctan (R_1'/L)\}. \qquad (14)$$

The first order or paraxial approximation of (14), valid when $R_1' \ll L$, is

$$r_o = bL/R_1'.$$

Electrons between r_o and R will strike C_1 if $\phi \geq \psi$, where

$$\tan \psi = (R_1 - r)/L.$$

That is, to first order approximation, electrons will strike C_1 if

$$r^2 - R_1 r + bL \geq 0.$$

The equality has the roots

$$r_1 = \frac{1}{2} R_1 - \frac{1}{2} R_1(1 - 4\, bL/R_1^2)^{1/2} \cong bL/R_1 \qquad (15a)$$

$$r_2 = \frac{1}{2} R_1 + \frac{1}{2} R_1(1 - 4\, bL/R_1^2)^{1/2} \cong R_1 - bL/R_1. \qquad (15b)$$

Four r ranges are thus specified. Electrons initially in the range $0 < r < r_o$ will not strike C_1 because their deflection ϕ is too large. Electrons in the range $r_o < r < r_1$ will strike C_1 because they pass near the scattering particle and obtain sufficient deflection. Electrons in the range $r_1 < r < r_2$ will not strike C_1 because their deflection is too small. Electrons in the range $r_2 < r < R$ (assuming $r_2 < R$) will strike C_1 because they require only a small deflection.

As a numerical example, consider the case where $L/R_1 = 100$, $R_1'/R_1 = 10$ and $\frac{1}{2} mu^2 = 1$ eV. Calculated values of b, r_o, r_1, r_2 and scattered electron current I_1 are shown in Table 4 for various N values.

These calculated data show several interesting results. First, water droplets can be charged to below their Rayleigh limit, shown as N in Table 4 for droplet radius r_{RL} (46), and cause significant scattering of the electron beam down to droplet diameters of 10^{-6} cm. Thus, water droplets of this size and larger seem to be detectable by electron beam scattering.

Second, the distance of nearest approach b between an electron and a droplet charged to near its Rayleigh limit exceeds the particle radius by an order of magnitude and since r_o exceeds b, Rutherford's scattering theory based on the assumption of coulombic interaction of point charges seems to be an adequate approximation for all electrons having $r > r_o$, i.e., for all electrons reaching the collectors C_1 and C_2.

Third, because $R_1 - r_2 = r_1$ is small except when N becomes quite large, a preferred detector design would not attempt to collect scattered electrons on C_1 from the outer annulus $r_2 < r < R$ because this would require the electron beam radius R to be nearly as large as R_1. In this case, background noise due to poorly collimated or unfocused electrons and to space charge expansion of the electron beam would probably cause poor signal to noise ratio (SNR). An optimum SNR value can only be obtained by both minimizing the background noise level and maximizing the signal level. (The importance of the

former has sometimes been overlooked in light scattering systems.) We therefore require R to be significantly less than R_1 which generally eliminates a scattered electron signal from the outer annulus $r_2 < r < R$, since $r_2 > R$.

Fourth, because r_1 exceeds r_o by an order of magnitude the scattered electron signal current I_1 is adequately given by

$$I_1 = \pi(bL/R_1)^2 I_o \tag{16}$$

where I_1 is the current density (amps/cm^2) at the electron beam axis.

A similar analysis of the scattering from a sheet electron beam passing through a slit of width 2t in the collector, analogous to the orifice of diameter 2 R_1 in collector C_1, gives the scattered electron signal

$$I_1 = \pi/2\ (bL/t)^2 I_o \tag{17}$$

which is exactly one-half that derived above for a circular beam with $R_1 = t$. Thus, the scattered electron signals from a sheet electron beam have comparable magnitude to those for a circular electron beam.

The electron beam current density I_o cannot be very large in a narrow, low energy beam like the one we are considering because space charge expansion of the beam occurs too quickly at large I_o. At a beam energy of 1 eV and current density I_o of 30 μamp/cm^2 the electron beam experiences negligible expansion over a path length L of 1 cm. Beyond this distance space charge expansion of the beam is rapid. A current density of this magnitude is easily obtainable, even by thermal electron emission which is space charge limited at low beam energies (62). A current density of I_o = 32 μamp/cm^2 was assumed in calculating the signal currents I_1 of Table 4.

Of course space charge expansion of the electron beam can be reduced by increasing the electron velocity. For sufficiently small expansion (small L), the beam expansion is given by the first order approximation (62-64)

$$\Delta R/R_i = I_o e\ L^2/(4\epsilon m u^3) \propto I_o/u^3 \tag{18}$$

where ΔR is the increase in beam radius over the initial radius R_i and ε the permittivity of vacuum. This idealized expression was obtained by solving Newton's law for a parallel, circular electron beam having uniform current density and electron energy. It is valid when

$$L < \left[\frac{\varepsilon m u^3}{I_o e}\right]^{1/2}$$

since higher order terms become important for larger L values.

According to expression (16) the signal current increases with beam energy according to

$$I_1 = \pi\left(\frac{2Ne^2L}{R_1 mu^2}\right)^2 I_o \propto I_o/u^4.$$

Thus, increase in both I_o and u so as to maintain constant signal I_1 always causes an increase in space charge expansion of the electron beam according to (18). Nevertheless, an electron beam energy somewhat higher than 1 eV may be optimum because higher energy beams can be better focused. Of course, the above analysis assuming point charge interaction only applies for beams of sufficiently low energy.

The signal currents of Table 4 cannot be detected without amplification. If the collector C_1 is an electron multiplier, amplification of 10^8 and sometimes 10^9 is possible. (However, acceleration of the scattered electrons may be required to induce secondary emission in the multiplier.) A gain of 10^7 together with a load resistance of 100 Ω would give voltage pulses of maximum amplitude between 1 mV and 10 V. Since the current density distribution is approximately Gaussian in electron beams (61), the resulting current or voltage signals will be roughly Gaussian of width equal to the particle TOF through the electron beam.

Although we have ignored complexities such as electron beam convergence, divergence and other distortions (64,66,67), background and shot noise and saturation of the electron multiplier, the foregoing prototype calculations suggest the detection of charged aerosol beam particles by electron beam scattering is a feasible technique for water droplet diameters $\geq$ .01 μm and for even smaller solid particles.

The calculations therefore suggest the TOFABS technique for measuring aerosol size distributions, previously demonstrated for particles > 0.3 μm, should be usable with electron beam detection for measuring size distributions over a much broader range. Although substantial development work remains, it

seems justified by these results and the need for a single instrument capable of rapid, accurate measurement of the particle size distribution over the size range from 0.01 to 10 μm.

Acknowledgement: The author is pleased to acknowledge the assistance of Dr. Yung Sung Cheng in collecting the references on velocity selectors and for helpful discussions on this subject and others, and of Dr. Dilip Padliya who provided the calculations on which Figs. 2, 4-6 and Tables 2 and 3 were based, as well as helpful discussions. This paper is based on work partially performed under contract with the U.S. Energy Research and Development Administration at the University of Rochester Biomedical and Environmental Research Project and has been assigned Report No. UR-3490-1031. Partial support for the work this paper describes was provided in the form of research grants from the U.S. National Institute of Environmental Health Sciences and the U.S. Environmental Protection Agency.

References:

1. B. Dahneke, Nature Phys. Sci., 244, 54 (1973).
2. B. Dahneke, H. Flachsbart, F. J. Mönig and N. Schwarzer, in K. Karamcheti, Ed., Rarefied Gas Dynamics, Academic Press, New York - London, 1974, p. 197.
3. B. Dahneke, Aerosol Sci., 4, 147 (1973).
4. B. Dahneke and D. Padliya, "Nozzle-inlet Design for Aerosol Beam Instruments," in J. L. Potter, Ed., Rarefied Gas Dynamics, AIAA, New York, Part II (1976).
5. G. W. Israel and S. K. Friedlander, J. Colloid and Interface Sci., 24, 330 (1967).
6. B. Dahneke and H. Flachsbart, Aerosol Sci., 3, 345 (1972).
7. U. S. Patent 3,854,321.
8. J. Gspann and H. Vollmar, "Mass Dependent Molecular Beam Focusing by Cross-jet Deflection," in J. L. Potter, Ed., Rarefied Gas Dynamics, AIAA, New York, Part II (1976).
9. M. H. Schwartz and R. P. Andres, Aerosol Sci., 7, 281 (1976).
10. P. M. Marcus and J. H. McFee, in I. Estermann, Ed., Recent Research in

Molecular Beams, Academic Press, New York, 1959, p. 43.

11. H. V. Hostettler and R. B. Bernstein, Rev. Sci. Instr., 31, 872 (1960).
12. S. M. Trujillo, P. K. Rol and E. W. Rothe, Rev. Sci. Instr., 33, 841 (1962).
13. J. L. Kinsey, Rev. Sci. Instr., 37, 61 (1966).
14. A. E. Grosser, Rev. Sci. Instr., 38, 257 (1967).
15. A. E. Grosser and R. B. Bernstein, "Compact Molecular Beam Velocity Selector," AEC Report COO-1328-15, Sept. 1965.
16. E. T. Manista, J. W. Sheldon and R. F. Fischer, J. Phys. E: Sci. Instr., 3, 395 (1971).
17. R. van Steyn and N. F. Verster, J. Phys. E: Sci. Instr., 5, 691 (1972).
18. D. J. Croucher and K. Lamb, J. Phys. E: Sci. Instr., 7, 735 (1973).
19. M. A. Platkov and S. V. Illarionov, Inst. Exp. Tech. 352 (1962).
20. A. Kristensen and R. L. Palmer, Rev. Sci. Instr., 38, 987 (1967).
21. M. J. Cardillo, M. S. Choy, E. F. Greene and D. B. Sheen, J. Chem. Phys., 7, 3054 (1971).
22. N. B. Johnson and R. A. Heppny, Rev. Sci. Instr., 41, 777 (1970).
23. D. R. Frankl, Rev. Sci. Instr., 45, 1375 (1974).
24. J. G. Dash and H. S. Sommers, Jr., Rev. Sci. Instr., 24, 91 (1953).
25. G. D. Este, B. Hilko, D. Sawyer and G. Scolis, Rev. Sci. Instr., 46, 223 (1975).
26. R. C. Miller and P. Kusch, Phys. Rev., 99, 1314 (1955).
27. L. T. Cowley, M. A. Fluendy and K. P. Lawley, Rev. Sci. Instr., 41, 666 (1970).
28. E. P. Pavlov and V. D. Perminov, J. Applied Mechanics and Techn. Phys., 480 (1972).
29. E. P. Borovkov and E. P. Pavlov, Instr. Exp. Tech., 15, 1494 (1972).
30. W. S. Young, Rev. Sci. Instr., 44, 715 (1973).
31. W. S. Young, J. Appl. Phys., 46, 3888 (1975).
32. G. W. Israel and J. S. Whang, in H. M. Englund and W. T. Beery, Eds., Proceedings of the 2nd International Clean Air Congress, Academic Press, New York, 1971. See also G. W. Israel and J. S. Whang, "Dynamical Properties of Aerosol Beams," Technical Note BN-709, Institute for Fluid Dynamics and Applied Mathematics, University of Maryland, College Park, July, 1971.

33. J. Gebhart, J. Heyder, C. Roth and W. Stahlhofen, in B. Y. H. Liu, Ed., Fine Particles, Academic Press, New York, 1975, p. 794.
34. W. Holländer and J. Schörmann, Atmos. Environ., 8, 817 (1974).
35. A. P. Avy and M. Benarie, Staub, 24, 343 (1964).
36. M. Benarie and J. P. Quetier, Aerosol Sci., 1, 77 (1970).
37. J. D. Hepburn, F. S. Chute and F. E. Vermeulen, A.I.A.A. Journ., 11, 370 (1973).
38. J. D. Hepburn, F. S. Chute and F. E. Vermeulen, A.I.A.A. Journ., 13, 249 (1975).
39. R. L. Myers and W. L. Fite, Environ. Sci. Techn., 9, 334 (1975).
40. W. D. Davis, "Continuous Mass Spectrometric Analysis of Particulates using Surface Ionization," Report No. 76CRD069, General Electric Corporate Research and Development, Schenectady, April 1976.
41. B. Dahneke, J. Colloid Interface Sci., 45, 584 (1973).
42. B. Dahneke, J. Colloid Interface Sci., 51, 58 (1975).
43. W. Holländer and J. Schörmann, private communication.
44. B. Dahneke, J. Colloid Interface Sci., 37, 342 (1971).
45. M. Dole, L. L. Mack, R. L. Hines, R. C. Mobley, L. D. Ferguson and M. B. Alice, J. Chem. Phys., 49, 2240 (1968).
46. K. T. Whitby and B. Y. H. Liu, in C. N. Davies, Ed., Aerosol Science, Academic Press, New York, 1966, p. 59.
47. B. J. Mason, Clouds, Rain and Rainmaking, Cambridge University Press, 1962.
48. T. D. Hall and W. W. Beeman, J. Applied Phys., 47, 5222 (1976).
49. O. F. Hagena, in P. P. Wegener, Ed., Molecular Beams and Low Density Gasdynamics, Marcel Dekker, New York, 1974, p. 93.
50. K. T. Dolder, Contemp. Phys., 17, 237 (1976).
51. B. Dahneke, Aerosol Sci., 4, 139 (1973).
52. B. Dahneke, Aerosol Sci., 4, 163 (1973).
53. H. Schlichting, Boundary Layer Theory, McGraw-Hill, New York, 1955.
54. T. T. Mercer, Aerosol Technology in Hazard Evaluation, Academic Press, New York, 1973.
55. B. Dahneke and S. Friedlander, Aerosol Sci., 1, 325 (1970).
56. A. H. Shapiro, The Dynamics and Thermodynamics of Compressible Fluid Flow, Vol. 1, Ronald Press, New York, 1953.

57. H. Ashkenas and F. Sherman, in J. H. de Leeuw, Ed., Rarefied Gas Dynamics, Vol. 2, Academic Press, New York, 1966.
58. J. B. French, A.I.A.A. Journ., 3, 993 (1965).
59. J. B. Anderson, in P. P. Wegener, Ed., Molecular Beams and Low Density Gasdynamics. Marcel Dekker, New York, 1974, p. 1.
60. R. H. Edwards, in J. L. Potter, Ed., Rarefied Gas Dynamics, AIAA, New York, Part I (1976).
61. H. Moss, Narrow Angle Electron Guns and Cathode Ray Tubes, Supplement 3 of "Advances in Electronics and Electron Physics," Academic Press, New York, 1968.
62. K. R. Spangenberg, Vacuum Tubes, McGraw-Hill, New York, 1948.
63. O. Klemperer, Electron Optics, 3rd edition, Cambridge University Press, 1971.
64. A. B. El-Kareh and J. C. J. El-Kareh, Electron Beams, Lenses and Optics, Vols. 1 and 2, Academic Press, New York, 1970.
65. E. Rutherford, Philos. Mag., Series VI, 21, 669 (1911).
66. C. C. Cutler, J. Appl. Phys., 27, 1028 (1956).
67. R. L. Kyhl and H. F. Webster, IRE Trans. of the Professional Group on Electron Devices, ED-3, 172 (1956).

Table 1 Compounds detected in airborne particulates by Davis (40) using surface ionization mass spectrometry.

Acetone	Nicotine	Cr_2O_3
Toluene	Camphor	Pb_3O_4
Mesitylene	Cinchonine	$NiSO_4$
Naphthalene	Uranyl Acetate	MgO
Dimethylnaphthalene	$CsNO_3$	Li_2O
Pyrene	$BaCO_3$	CCl_4
Ethyl Alcohol	$BiCO_3$	CuO
t-Butyl Alcohol	$CaCO_3$	MoO
Aniline	$SrCO_3$	

Table 2 Calculated gas velocities and properties and the calculated particle velocities that result for unit density spheres. These data apply for nozzle 1 of Fig. 4 except for a 0.1 mm length of constant diameter at the nozzle exit not present in nozzle 1.

Distance from nozzle inlet plane, mm	Gas velocity and properties				Particle velocity		
	V, M/sec	M -	T, °K	P, Torr	d = 0.1 μm M/sec	d = 1.0 μm M/sec	d = 10. μm M/sec
0.1	2.07	.006	293.0	730.0	2.06	2.00	1.08
0.3	4.94	.014	293.0	729.9	4.93	4.65	1.97
0.5	10.86	.032	292.9	729.5	10.82	9.70	3.47
0.7	24.07	.070	292.7	727.5	23.87	19.61	6.08
0.9	54.42	.159	291.5	717.2	53.43	38.56	11.12
1.1	120.46	.355	285.8	669.0	116.02	73.45	21.18
1.3	238.36	.731	264.7	511.8	223.09	129.03	38.77
1.5	313.27	1.000	244.2	385.6	310.74	188.80	59.50
1.7	571.93	2.500	130.2	42.7	439.79	238.54	76.00
1.9	663.82	3.856	73.7	5.8	478.97	255.93	82.59
2.1	700.48	5.000	48.8	1.4	489.50	260.46	84.84
2.3	716.89	5.858	37.3	0.5	493.46	262.11	85.77
2.5	724.46	6.404	31.8	0.3	495.60	262.99	86.27

Table 3 Calculated increase in particle diameter due to condensational growth. The various vapors were added to an air aerosol so that the mixture was at NTP and the partial pressure of the vapor equalled its saturation pressure.

Condensible Vapor	Vapor Pressure at 293 °K (Torr)	Final Diameter for Initial Particle Diameter of: 0.5 μm (μm)	0.1 μm (μm)
Water	17.404	0.5004	0.1004
Acetone	177.810	0.5084	0.1080
Benzene	74.662	0.5007	0.1007
Ethanol	42.947	0.5021	0.1021

Table 4 Calculated values for a circular electron beam scattered by a particle at its center having N electronic charges.

N	r_{RL}, cm	b, cm	r_o, cm	$r_1=R_1-r_2$, cm	I_1, μamp
10	2×10^{-7}	1.44×10^{-6}	1.45×10^{-5}	1.44×10^{-4}	2.56×10^{-6}
20	3×10^{-7}	2.88×10^{-6}	2.89×10^{-5}	2.88×10^{-4}	1.02×10^{-5}
50	5×10^{-7}	7.20×10^{-6}	7.20×10^{-5}	7.20×10^{-4}	6.40×10^{-5}
100	8×10^{-7}	1.44×10^{-5}	1.45×10^{-4}	1.44×10^{-3}	2.56×10^{-4}
200	1×10^{-6}	2.88×10^{-5}	2.89×10^{-4}	2.88×10^{-3}	1.02×10^{-3}
500	2×10^{-6}	7.20×10^{-5}	7.20×10^{-4}	7.20×10^{-3}	6.40×10^{-3}
1000	4×10^{-6}	1.44×10^{-4}	1.44×10^{-3}	1.44×10^{-2}	2.56×10^{-2}

$L/R_1 = 100$, $L/R_1' = 10$, $I_o = 32$ μamp/cm^2, $\frac{1}{2}mu^2 = 1$ eV

$r_{RL} = [Ne/\sqrt{16\pi\sigma}]^{2/3}$, $\sigma = 75.6$ dynes/cm.

Figure 1 Comparison of measured and calculated particle velocities in an aerosol beam generated by expansion of latex sphere aerosols at NTP through a converging nozzle 2.1 mm long and 0.4 mm in diameter. A normal shock was assumed just upbeam of a collimator located 2 mm from the nozzle exit plane. The shock wave location was selected to give the best agreement of the calculated and measured data.

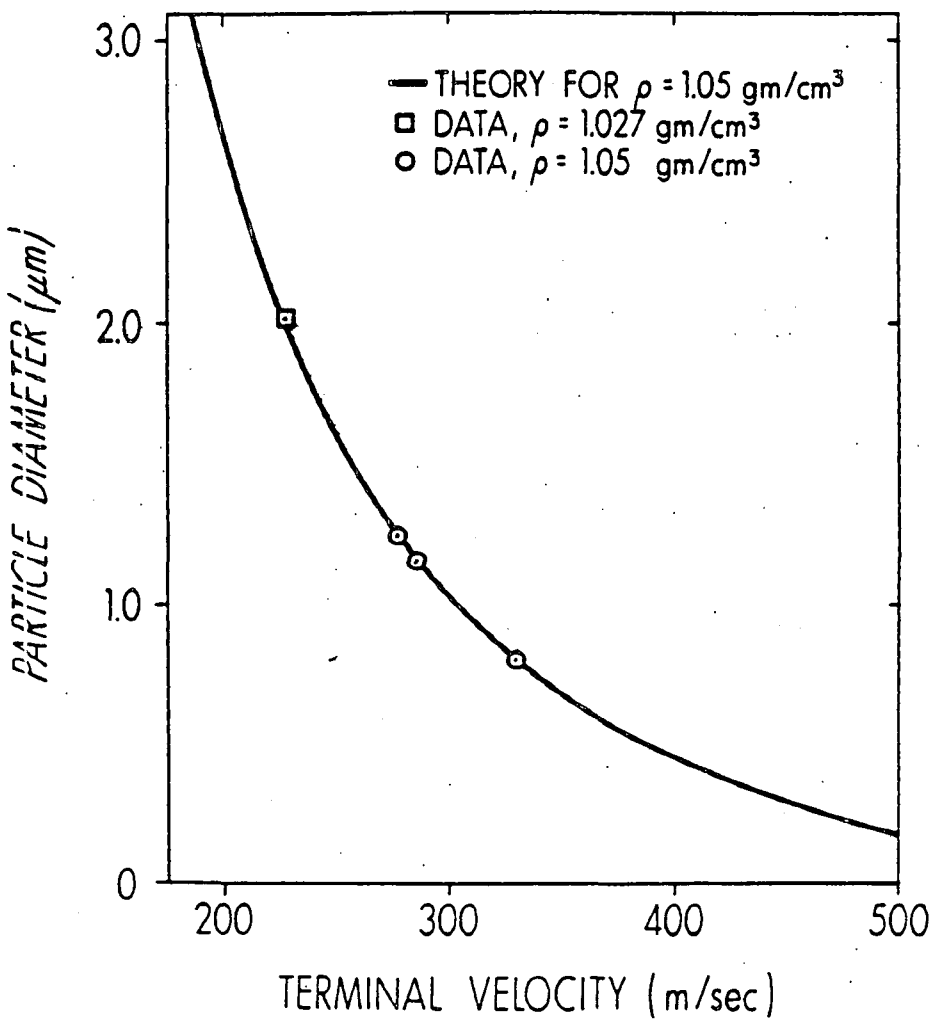

Figure 2 Comparison of measured and calculated particle TOF through a focused laser beam. The laser beam thickness of 72 μm was assumed because it gave best agreement between the measured and calculated data. The beam was generated by expansion of latex sphere aerosols initially at NTP. These results are comparable to the data of Table 2.

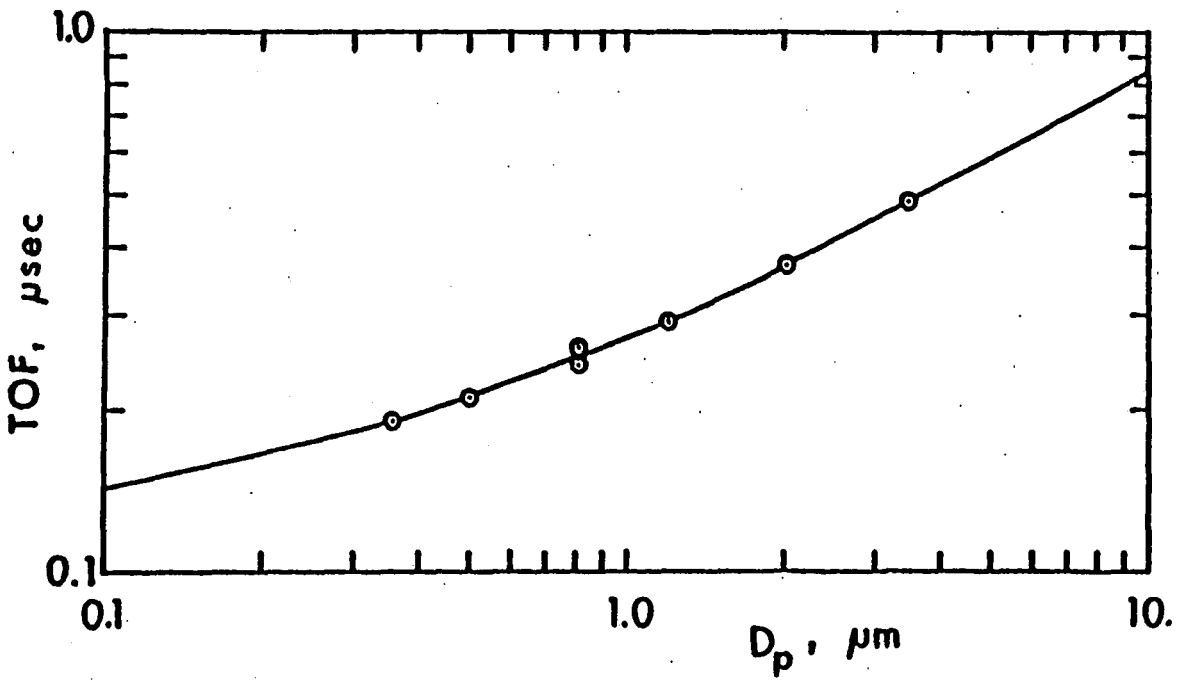

Figure 3 Measured particle velocities vs. particle diameter for beams of latex spheres generated by expanding helium and air aerosols at NTP through a capillary of 0.5 mm diameter and 300 mm length.

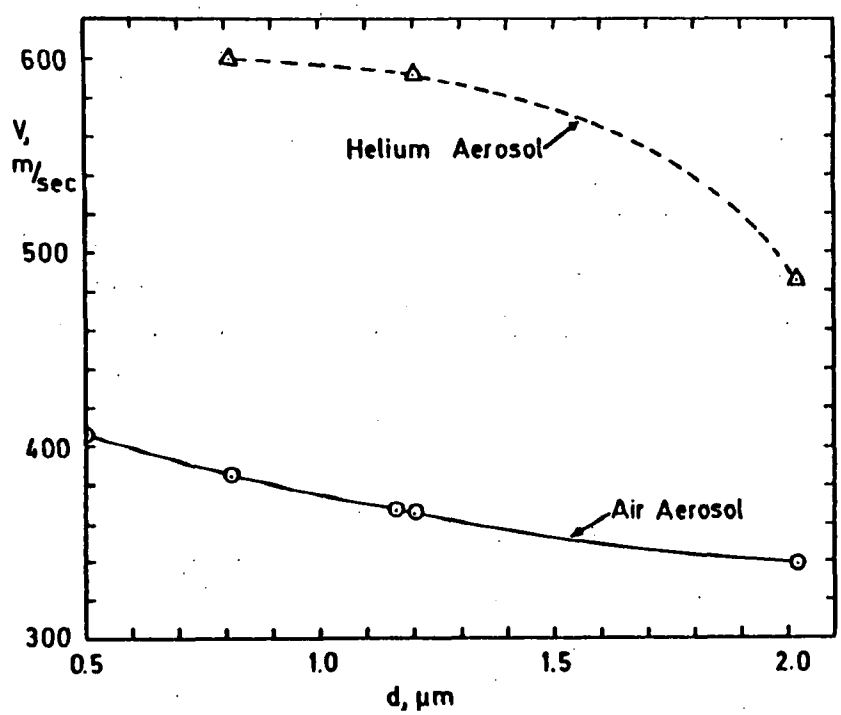

Figure 4 Calculated particle TOF vs. particle diameter for beams of unit density spheres generated by assumed expansion of air aerosols at NTP through the three nozzles specified. A flight path of 100 μm beginning 2 mm from the nozzle exit plane was assumed.

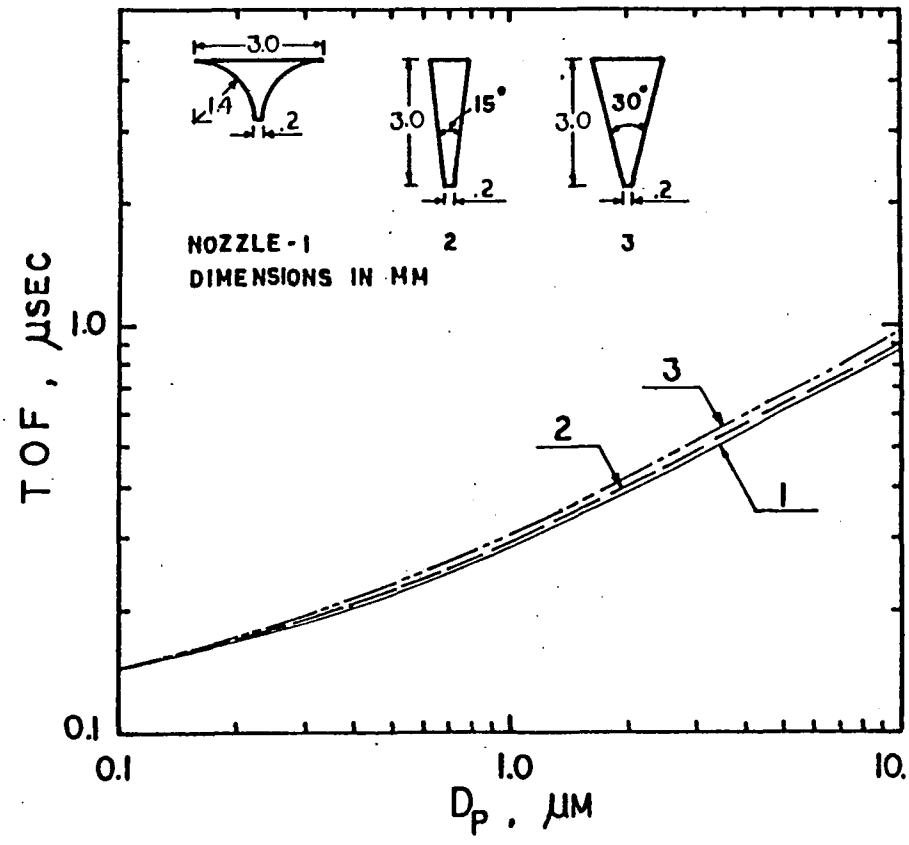

Figure 5 Calculated particle TOF vs. particle diameter for nozzle 2 of Figure 4 with three nozzle diameters. An air aerosol at NTP containing unit density spheres was assumed expanded through the nozzle to generate the beam. The TOF was calculated for a flight path of 100 μm beginning 2 mm from the nozzle exit plane.

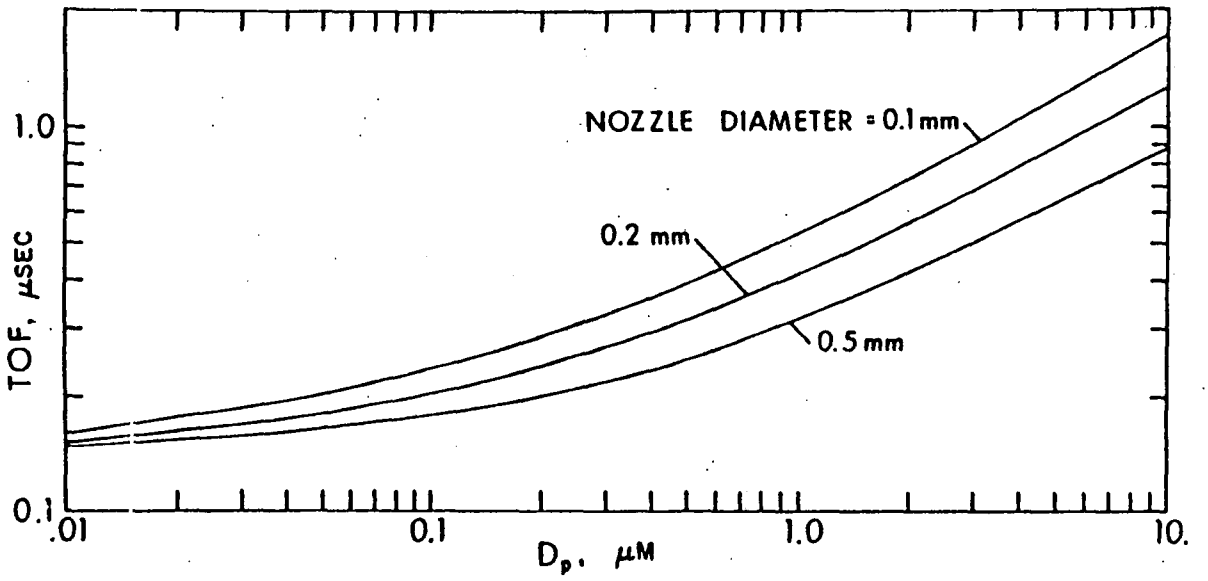

Figure 6 Calculated particle TOF vs. particle diameter for assumed expansion of air aerosols at NTP containing spheres at the three mass densities shown through nozzle 2 of Fig. 4. Particle TOF was calculated for a flight path of 100 μm beginning 2 mm from the nozzle exit plane.

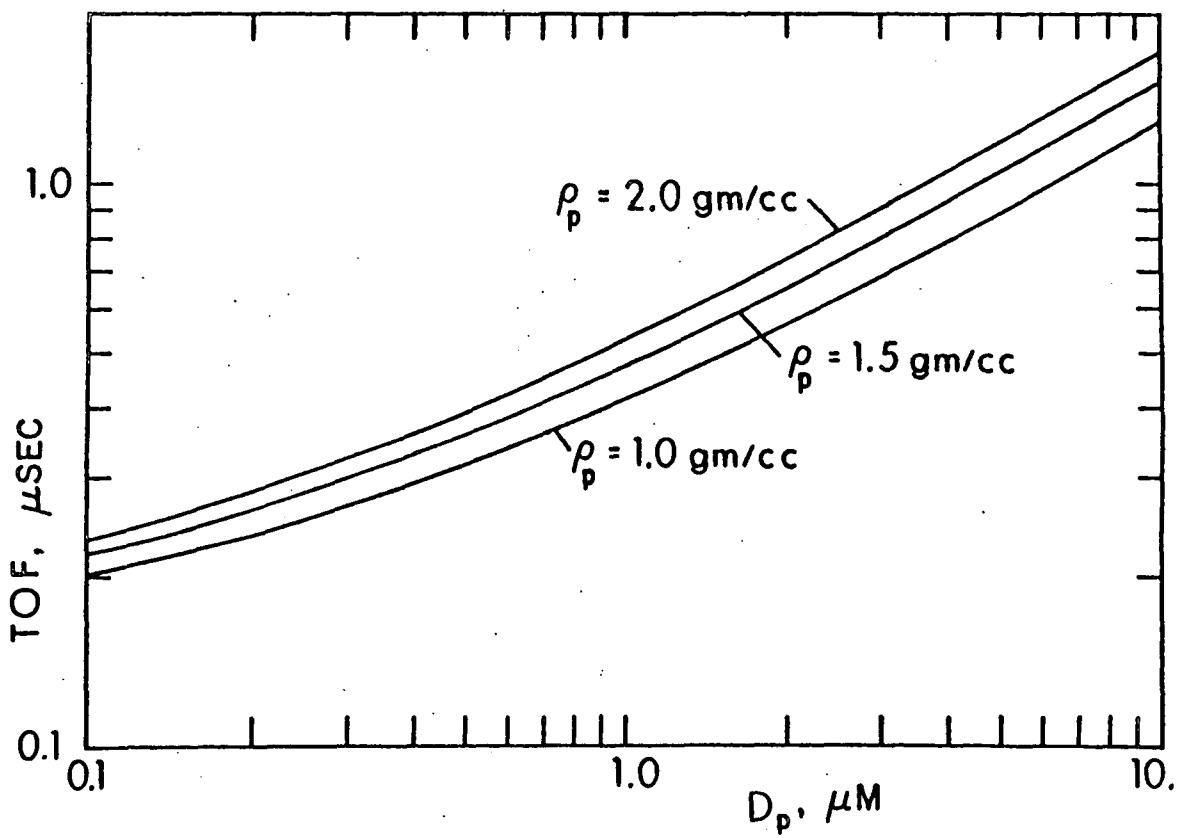

Figure 7 Measured beam diameter D_b vs. particle diameter D_p for beams of latex spheres generated in a converging nozzle of 0.4 mm throat diameter, 2.1 mm length and total flow of 1390 cc of air at NTP per min. Open and closed circles represent beam diameters at 10 and 20 mm from the nozzle exit plane, respectively. Beam diameter was reduced an order of magnitude by restricting the aerosol sample to a small central fraction (28 cc/min) of the total flow. Except for the smaller particle sizes in such focused beams, which apparently tend to unfocus by particle diffusion, the data all fit an expression of the form $D_b = D_o \exp(-mD_p)$ where D_o and m are constant.

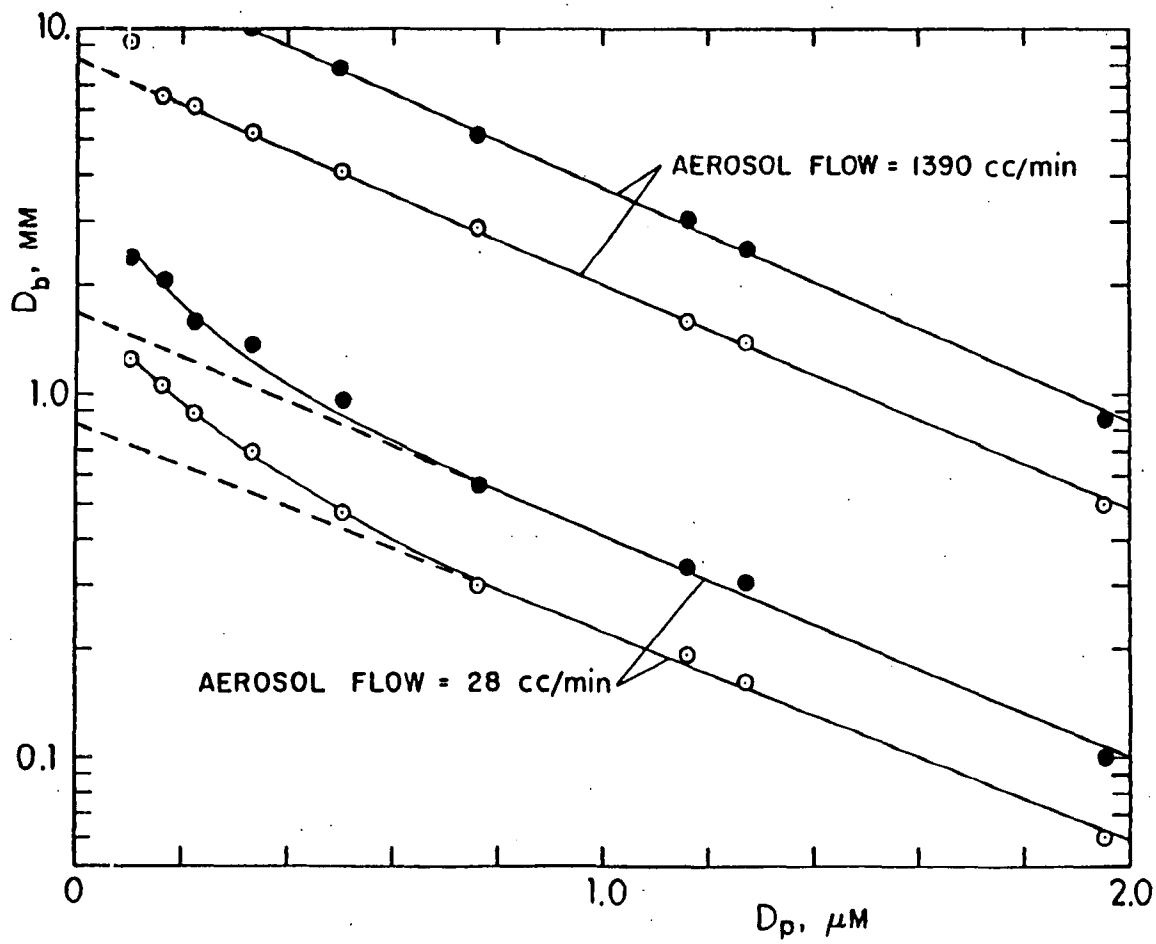

Figure 8 Frequency (no. of particles) vs. TOF for air aerosols at NTP containing uniform latex spheres of a single size and aggregates of these spheres. The unusually high fraction of aggregates was obtained by spraying undiluted aqueous suspensions of the spheres into an air stream.

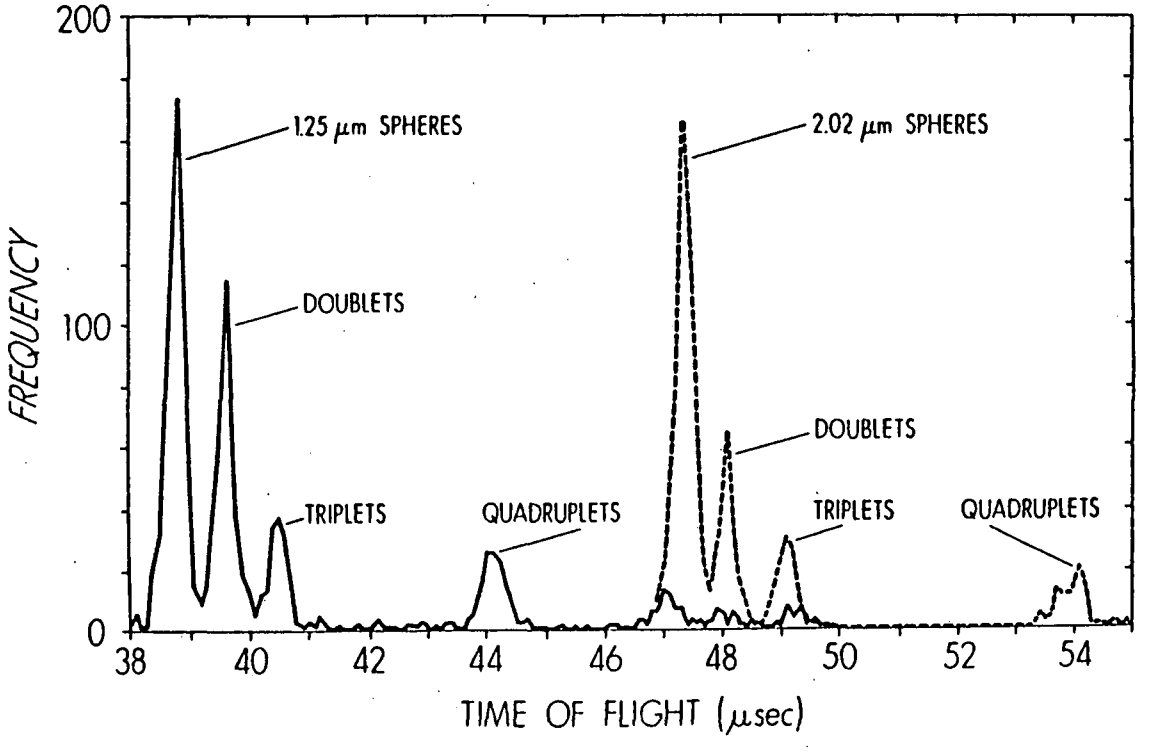

Figure 9 Schematic diagram of a time of flight aerosol beam spectrometer (TOFABS) using a single, focused laser beam to detect and measure airborne particles.

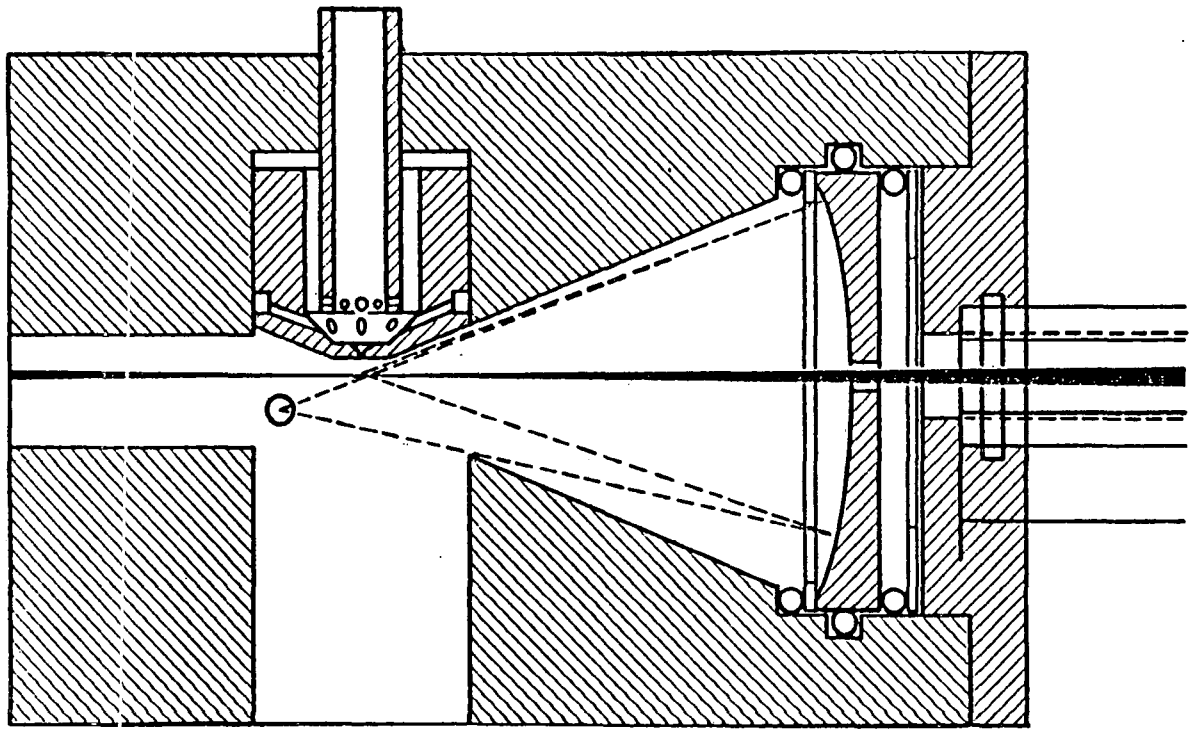

Figure 10 Upper oscilloscope trace: superimposed PMT signals generated by the light scattered as 2.02 μm diameter latex spheres traverse the focused laser beam. The horizontal scale is 0.2 μsec per major division. Lower trace: superimposed logic pulses of fixed amplitude and width equal to particle TOF through the laser beam. The logic pulse time scale is delayed 0.5 μsec relative to the PMT signal.

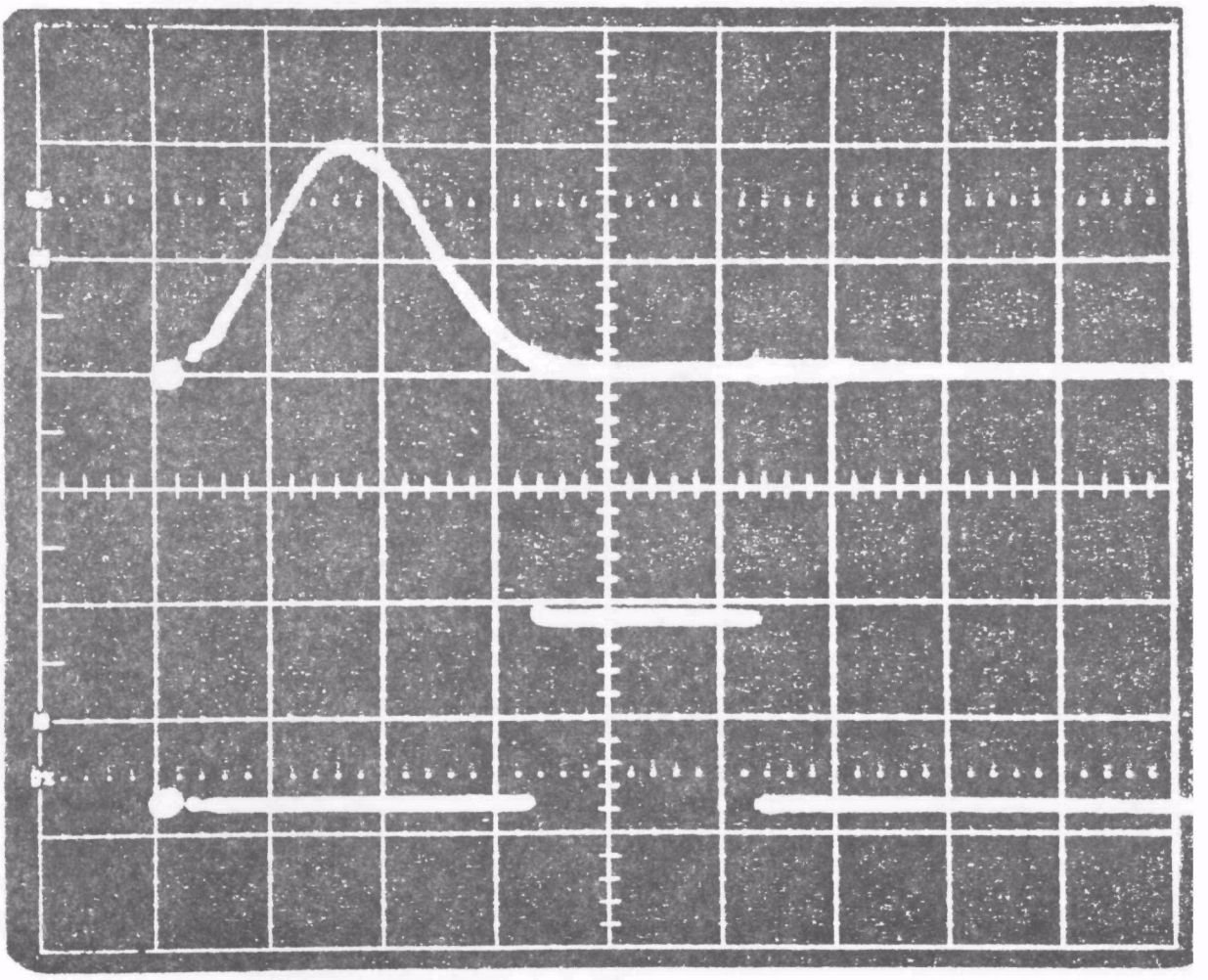

Figure 11 Schematic diagram of the electronics system that processes the PMT signals of Fig. 10 to obtain the logic pulses of Fig. 10 and stores and displays the data as shown in Fig. 12.

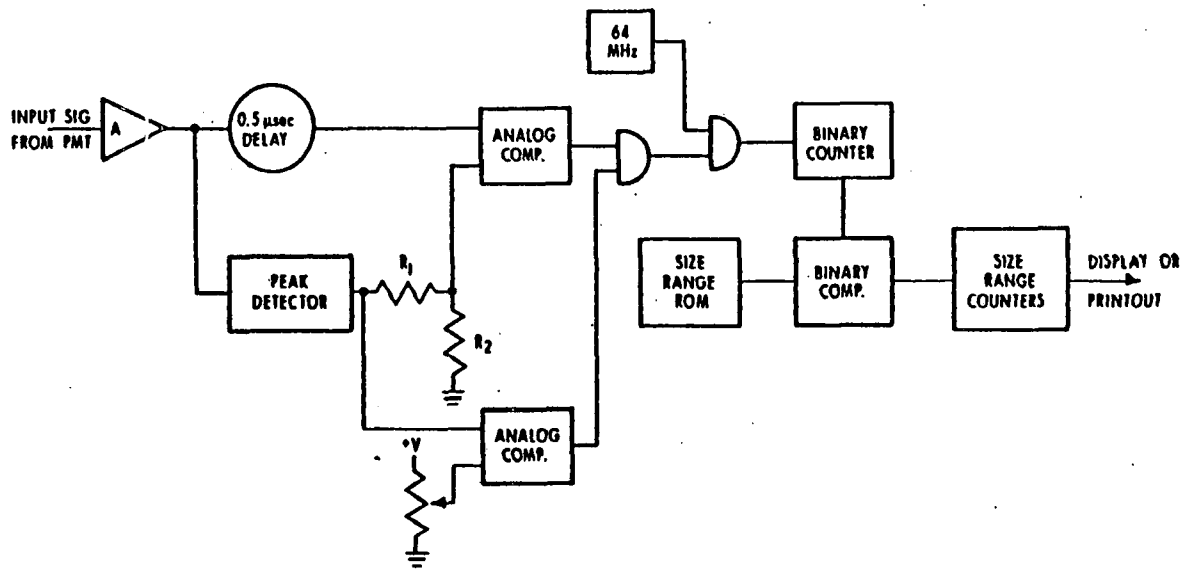

Figure 12 Measured TOF distribution for a polydisperse NaCl aerosol. Vertical axis is number of particles while horizontal axis is TOF. The maximum corresponds to an aerodynamic diameter of 0.9 μm, that is, a unit density sphere of this diameter will obtain the same TOF.

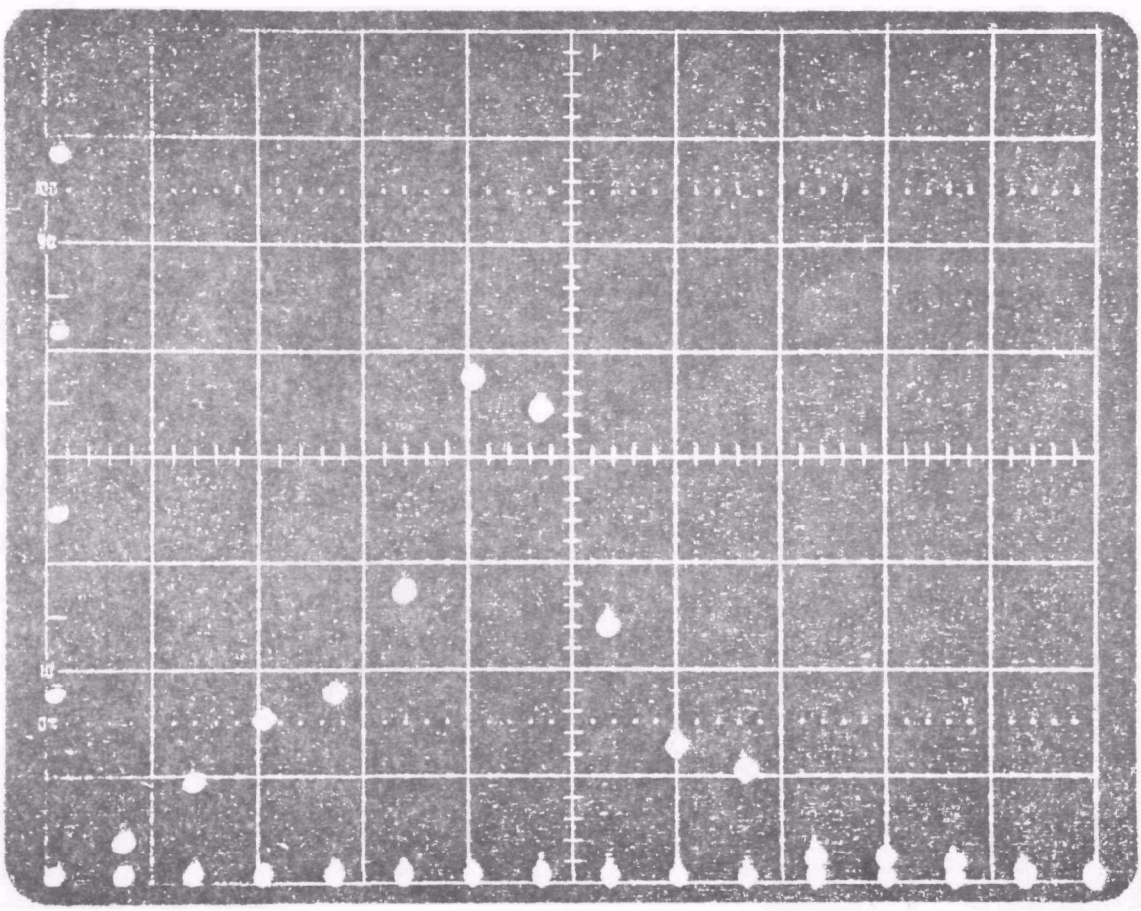

Figure 13 Schematic diagram of a scattered electron beam detector. Aerosol beam particles previously charged in passing through an electron beam can be detected in passing through subsequent electron beams because the charged particles scatter electrons onto the collector (electron multiplier) C_1.

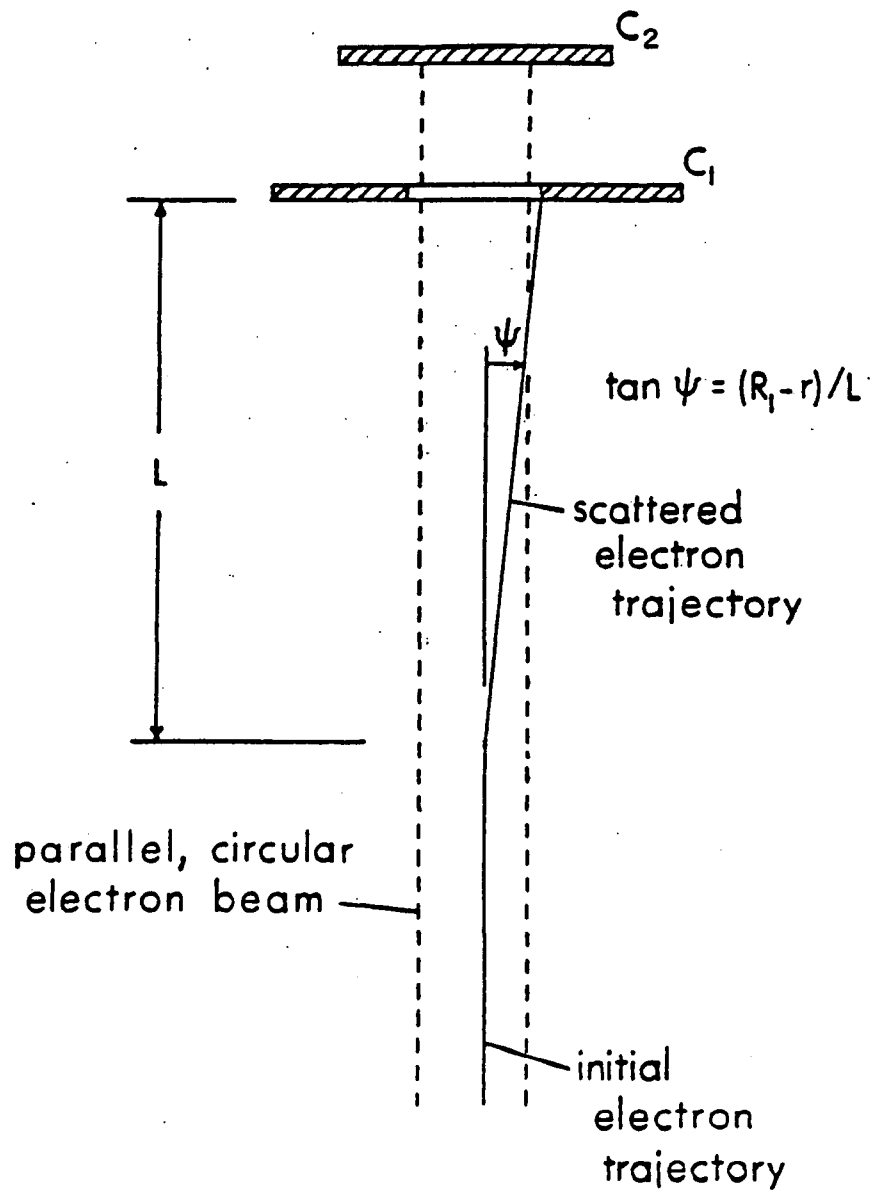

TECHNICAL REPORT DATA
(Please read Instructions on the reverse before completing)

1. REPORT NO.	2.	3. RECIPIENT'S ACCESSION NO.
EPA-600/2-77-229		

4. TITLE AND SUBTITLE	5. REPORT DATE
TIME-OF-FLIGHT AEROSOL BEAM SPECTROMETER FOR PARTICLE SIZE MEASUREMENTS	November 1977
	6. PERFORMING ORGANIZATION CODE
7. AUTHOR(S)	8. PERFORMING ORGANIZATION REPORT NO.
Barton Dahneke	
9. PERFORMING ORGANIZATION NAME AND ADDRESS	10. PROGRAM ELEMENT NO.
Department of Radiation Biology and Biophysics University of Rochester Rochester, New York 14642	1AD712, BE-23 (FY 77)
	11. CONTRACT/GRANT NO.
	R803065
12. SPONSORING AGENCY NAME AND ADDRESS	13. TYPE OF REPORT AND PERIOD COVERED
Environmental Sciences Research Laboratory - RTP, NC Office of Research and Development U.S. Environmental Protection Agency Research Triangle Park, N.C. 27711	FINAL 6/74 - 3/77
	14. SPONSORING AGENCY CODE
	EPA/600/09

15. SUPPLEMENTARY NOTES

16. ABSTRACT

A time-of-flight aerosol beam spectrometer (TOFABS) is described. The instrument has been designed and constructed to perform in situ real time measurements of the aerodynamic size of individual aerosol particles in the range 0.3 to 10 μm diameter. The measurement method consists of (1) allowing a sample aerosol to undergo expansion through a nozzle into a vacuum chamber, such that each particle acquires a terminal velocity depending on its aerodynamic size, then (2) measuring the terminal velocity by determining the time taken for each particle to traverse a laser beam of fixed width. An experimental calibration curve relating time-of-flight and aerodynamic size, based on the use of polystyrene latex spheres, is shown to be in good agreement with a theoretical calibration obtained from the gas - particle dynamics equations. A comprehensive discussion of the properties and uses of aerosol beams is included as an appendix.

17. KEY WORDS AND DOCUMENT ANALYSIS

a. DESCRIPTORS	b. IDENTIFIERS/OPEN ENDED TERMS	c. COSATI Field/Group
*Air pollution		13B
*Aerosols		07D
*Particle size distribution		20D
Aerodynamic characteristics		
Rarified gas dynamics		
Stokes law		

18. DISTRIBUTION STATEMENT	19. SECURITY CLASS *(This Report)*	21. NO. OF PAGES
RELEASE TO PUBLIC	UNCLASSIFIED	93
	20. SECURITY CLASS *(This page)*	22. PRICE
	UNCLASSIFIED	

EPA Form 2220-1 (9-73)